



CHORUS

This is the accepted manuscript made available via CHORUS. The article has been published as:

Class of topological phase transitions of Rashba spin-orbit coupled fermions on a square lattice

Yu Yi-Xiang, Fadi Sun, and Jinwu Ye

Phys. Rev. B **98**, 174506 — Published 19 November 2018

DOI: [10.1103/PhysRevB.98.174506](https://doi.org/10.1103/PhysRevB.98.174506)

New class of topological phase transitions of Rashba spin-orbit coupled fermions on a square lattice

Yu Yi-Xiang^{1,2}, Fadi, Sun^{3,4,5}, and Jinwu Ye^{3,4,5}

¹ *Beijing National Laboratory for Condensed Matter Physics,*

Institute of Physics, Chinese Academy of Sciences, Beijing 100190, China

² *School of Physical Sciences, University of Chinese Academy of Sciences, Beijing 100190, China*

³ *Department of Physics, Capital Normal University,*

Key Laboratory of Terahertz Optoelectronics, Ministry of Education,

and Beijing Advanced Innovation Center for Imaging Technology, Beijing, 100048, China

⁴ *Department of Physics and Astronomy, Mississippi State University, P. O. Box 5167, Mississippi State, MS, 39762*

⁵ *Kavli Institute of Theoretical Physics, University of California, Santa Barbara, Santa Barbara, CA 93106*

(Dated: September 14, 2018)

We study the system of attractively interacting fermions hopping in a square lattice with any linear combinations of Rashba or Dresselhaus spin-orbit coupling (SOC) in a normal Zeeman field. By imposing self-consistence equations at half filling with zero chemical potential, we find there are 3 phases: Band insulator (BI), Superfluid (SF) and Topological superfluid (TSF) with a Chern number $C = 2$. The $C = 2$ TSF happens in small Zeeman fields and weak interactions which is in the experimentally most easily accessible regime. The transition from the BI to the SF is a first order one due to the multi-minima structure of the ground state energy landscape. There is a new class of topological phase transition (TPT) from the SF to the $C = 2$ TSF at the low critical field h_{c1} , then another one from the $C = 2$ TSF to the BI at the upper critical field h_{c2} . We derive effective actions to describe the two new classes of topological phase transitions, then use them to study the Majorana edge modes and the zero modes inside the vortex core of the $C = 2$ TSF near both h_{c1} and h_{c2} , especially explore their spatial and spin structures. We find the edge modes decay into the bulk with oscillating behaviors and determine both the decay and oscillating lengths. We compute the bulk spectra and map out the Berry Curvature distribution in momentum space near both h_{c1} and h_{c2} . We elaborate some intriguing bulk-Berry curvature-edge-vortex correspondences. We also discuss the competitions between SFs and charge density wave (CDW) states in more general cases. A possible classification scheme of all the TPTs in a square lattice is outlined. Comparisons with previous works on related systems are discussed. Possible experimental implications in cold atoms in an optical lattice are given.

I. INTRODUCTION

Since the experimental discovery of topological insulators^{1,2} and Weyl semi-metals³⁻⁸, it became a primary goal to find a first topological superfluid (TSF)^{1,2,9} in any experimental systems. The system of attractively interacting Rashba spin-orbit coupled fermions in a Zeeman field² was considered to be one of the most promising systems to experimentally realize a topological superfluid. It was theoretically studied in the context of the hetero-structure made of s-wave superconductor-noncentro-symmetric semiconductor- magnetic insulator (SM-SC-MI)¹¹⁻¹⁴. In this SC-SM-MI hetero-structure, the noncentro-symmetric semiconductor (SM) hosts a strong Rashba or Dresselhaus SOC, the superconductor provides the S-wave pairing to the SM due to its proximity effects, the MI induces a Zeeman field applied to the SM. Under the combined effects of the SOC, S-wave pairing and the Zeeman field, the SM sandwiched between the SC and MI may enter into a Chern number $C = 1$ TSF phase which hosts Majorana fermions in its vortex core. Unfortunately, so far the experimental results on the hetero-structure came out as negative.

It was well known that a lattice system may offer a new platform to host new phases and phase transitions. In this work, we study the system of attractively inter-

acting fermions at half filling with the chemical potential $\mu = 0$. subject to the Rashba spin-orbit coupling (SOC) hopping in a square lattice in a normal Zeeman field Eq.1. This system was first investigated in¹⁵ in the context of cold atoms loaded on an optical lattice and found to be a promising system to search for TSF in cold atom systems. Unfortunately, the self-consistent equations were ignored in¹⁵, so what are the ground states and phase transitions can not be determined, possible experimental implications are rather limited. In the cold atom systems¹⁰, it is difficult to construct such a SC-SM-MI hetero-structure, but one advantage over the structure is the absence of any orbital effects due to the charge neutrality of the cold atoms. Another advantage is that all relevant parameters are experimentally tunable. For example, the negative interaction $-U$ can be induced by a S-wave Feshbach resonance¹⁰. In view of the experimental advances over the previous 1d SOC¹⁶⁻¹⁸ to generate 2d Rashba SOC for the fermion ⁴⁰K gas^{19,20} to generate the tunable quantum anomalous Hall (QAH) SOC for ⁸⁷Rb atoms²¹, and also optical lattice clock scheme to generate very long lifetime 1d SOC for various atoms²²⁻²⁸, we hope 2d Rashba SOC with a long enough lifetime in a square lattice maybe generated in some near future cold atom experiments. The Zeeman field H and the number of atoms N can be easily controlled. A crucial question to

ask is what are the experimental conditions to observe a possible TSF in such a lattice system? If so, what are the properties of the TSF and associated topological phase transitions? To answer these questions, one must impose the self-consistent equations under the tunable experimental parameters such as the SOC strength and the parameters N, U, h to determine the ground states and phase transitions. We will try to achieve this goal in this paper.

In this paper, we find that it is very important to impose the self-consistency conditions which lead to the global phase diagram in Fig.1. For the isotropic Rashba SOC $\alpha = \beta$ (See Eq.1), there are three phases: a topological superfluid phase (TSF) with a high Chern number $C = 2$ at a small h and small U , a Band insulator (BI) at a large h and a normal SF at a large U . The transition from the BI to the SF at $h = h_b$ is a bosonic one with the pairing amplitude Δ as the order parameter. It is a first order one with meta-stable regimes on both sides of the transition (denoted by the two dashed lines) in Fig.1. The topological transition from the SF to the $C = 2$ TSF at $h = h_{c1}$ in Fig.1 is a fermionic one at the two Dirac points $(\pi, 0)$ and $(0, \pi)$ with no order parameter. It is a third order TPT in the first segment along h_{c1} , then turn into a first order one at the topological tri-critical point T , continue to the multi-critical point M . The transition from the $C = 2$ TSF to the BI at h_{c2} has both bosonic and fermionic nature, the bosonic sector has the pairing amplitude Δ as the order parameter representing the onset of the off-diagonal long range order of the $C = 2$ TSF, the fermionic sector happens at the two Dirac points $(0, 0)$ and (π, π) , representing the onset of the topological nature of the $C = 2$ TSF. The Berry curvature of the $C = 2$ TSF in momentum space are sharply peaked at $(0, \pi)$ and $(\pi, 0)$ near h_{c1} in Fig.3a, but are located around $(0, 0)$ and (π, π) near h_{c2} with the non-trivial structure shown in Fig.4a. In the $C = 2$ TSF, there are always $C = 2$ Majorana edge modes at $k_y = 0$ and $k_y = \pi$ respectively which decay into the bulk with an oscillating behavior. The two Majorana edge modes carry both spins near h_{c1} , but spin up and spin down at $k_y = 0$ and $k_y = \pi$ respectively near h_{c2} . There are $C = 2$ Majorana zero modes inside a vortex core which also show different spin structures near h_{c1} and h_{c2} . There are intriguing bulk energy spectrum-Berry curvature-edge state-vortex core relations. We also discuss its experimental realizations in cold atoms in an optical lattice.

Then we discuss the competitions between the SF and CDW in more general cases. We find that at half filling with the chemical potential $\mu = 0$, the SF and CDW are degenerate both at the mean field weak coupling BCS limit and in the leading order in the strong coupling BEC limit. So quantum fluctuations in the weak coupling BCS limit and the expansion to the next order to include the ring exchange term in the strong coupling BEC limit are needed to resolve the true quantum ground state. This is a manifestation of “the order from quantum disorder”

mechanism in fermionic systems. We expect this mechanism may likely favor SF over CDW. We find adding any chemical potential μ or a next nearest neighbour (NNN) hopping t' will favor the SF over the CDW even at the mean field weak coupling BCS limit and in the leading order in the strong coupling BEC limit. However, due to the changes of the symmetries, the phases with $\mu \neq 0$ or $t' \neq 0$ will be worked out in separate publications.

We consider the Hamiltonian of interacting two pseudo-spin (labeled as \uparrow and \downarrow) fermions hopping in the 2D square lattice subject to any linear combinations of Rashba and Dresselhaus SOC and a Zeeman field:

$$H = -t \sum_i \left[c_i^\dagger e^{i\alpha\sigma_x} c_{i+\hat{x}} + c_i^\dagger e^{i\beta\sigma_y} c_{i+\hat{y}} + h.c. \right] - \mu \sum_i c_i^\dagger c_i - h \sum_i c_i^\dagger \sigma_z c_i + U \sum_i c_{i\uparrow}^\dagger c_{i\downarrow}^\dagger c_{i\downarrow} c_{i\uparrow} \quad (1)$$

where $c_i^\dagger = \begin{bmatrix} c_{i\uparrow}^\dagger & c_{i\downarrow}^\dagger \end{bmatrix}$, $\sigma_{x,y,z}$ are three Pauli matrices, and \hat{x} and \hat{y} denote the unit vector in x and y direction respectively. The negative interaction $U < 0$ can be tuned by the Feshbach resonance in cold atoms or superconducting proximity effects in materials. The chemical potential μ should be determined by the filling factor $\nu = \frac{N}{2L_x L_y}$, where N is the number of fermions, L_x (or L_y) is the size of the system along x (or y) direction, and the factor 2 comes from the two spin species. We mainly focus on the half filling cases with the chemical potential $\mu = 0$. However, in Sec.VII, we will also stress the roles of $\mu \neq 0$ and $t' \neq 0$ when discussing the competitions between the SF and CDW.

The rest of the paper is organized as follows. In Sec.II, we present exact symmetry analysis on the Hamiltonian or its mean field form which will guide our qualitative physical pictures of the global phase diagram Fig.1. Then we explore the SF to the $C = 2$ TSF transition at h_{c1} in Sec.III and the $C = 2$ TSF to the BI transition at h_{c2} in Sec.IV. Then we use the effective actions near h_{c1} and h_{c2} derived in the previous two sections to study the spin and spatial structures of the edge modes in Sec.V and inside a vortex core in Sec.VI. In Sec.VII, we discuss the competition between the SF and the CDW state in both weak coupling BCS limit and strong coupling BEC limit in more general cases, stress the “order from disorder” mechanism for the fermionic systems at $\mu = 0, t' = 0$. In Sec. VIII, we make critical comparisons and discussions between the results achieved in this manuscript and those achieved in some previous works on related systems. In Sec.IX, we discuss the experimental realizations and detections of the $C = 2$ TSF in cold atoms loaded in an optical lattice. In the final Sec.X, we reach conclusions and elaborate several perspectives. Some technical details are given in the 3 appendices.

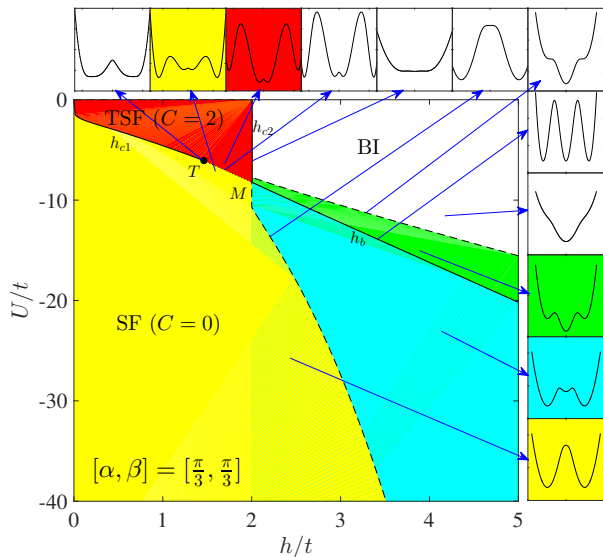


FIG. 1. The phase diagram of attractively interacting fermions with the Rashba SOC in a Zeeman h at half filling with the chemical potential $\mu = 0$. The SOC parameter is $[\alpha, \beta] = [\frac{\pi}{3}, \frac{\pi}{3}]$. The insets are the ground state energy E_G versus the bosonic SF order parameter Δ at each phase and phase boundary. The transition from the BI to the SF at h_b is a first order bosonic one with the superfluid order parameter Δ . The SF to $C = 2$ TSF transition at h_{c1} is a fermionic (topological) one with no order parameters. Along h_{c1} , it is third order from 0 to the topological Tri-critical point (T), then become first order from the T to the multi-critical point (M). The transition from the $C = 2$ TSF to the BI at h_{c2} has both bosonic and fermionic (topological) nature. The three lines h_{c1} , h_{c2} and h_b meet at the multi-critical point M. The h_{c2} is strictly straight, while h_{c1} is tangent to $h = 0$ axis near the origin.

II. EXACT SYMMETRY ANALYSIS AND QUALITATIVE PHYSICAL PICTURES.

The Zeeman field breaks the Time reversal symmetry. As usual, there is always a P-H symmetry on the BCS mean field Hamiltonian Eq.34: $CH_{MF}(\mathbf{k})C^{-1} = -H_{MF}(-\mathbf{k})$ which picks up the four P-H invariant momenta $(0, 0), (\pi, 0), (0, \pi), (\pi, \pi)$. The Hamiltonian Eq.1 also has the \mathcal{P}_z symmetry: $k_x \rightarrow -k_x, S^x \rightarrow -S^x, k_y \rightarrow -k_y, S^y \rightarrow -S^y, S^z \rightarrow S^z$ which is also equivalent to a joint π rotation of the spin and orbital around \hat{z} axis²⁹. This symmetry indicates $\sigma_z H(\mathbf{k}) \sigma_z = H(-\mathbf{k})$. It also picks up the same four P_z symmetric momenta³⁰.

At the isotropic Rashba limit $\alpha = \beta$, it has the enlarged $[C_4 \times C_4]_D$ symmetry which is also equivalent to a joint $\pi/2$ rotation of the spin and orbital around \hat{z} axis. This symmetry indicates the equivalence between $(0, \pi)$ and $(\pi, 0)$. The Hamiltonian is also invariant under $\alpha \rightarrow \pi - \alpha, k_x \rightarrow \pi - k_x$ and $\beta \rightarrow \pi - \beta, k_y \rightarrow \pi - k_y$. At the extremely anisotropic limit ($\alpha = \pi/2, \beta$), it indicates the equivalence between $(0, 0)$ and $(\pi, 0)$, also between $(0, \pi)$

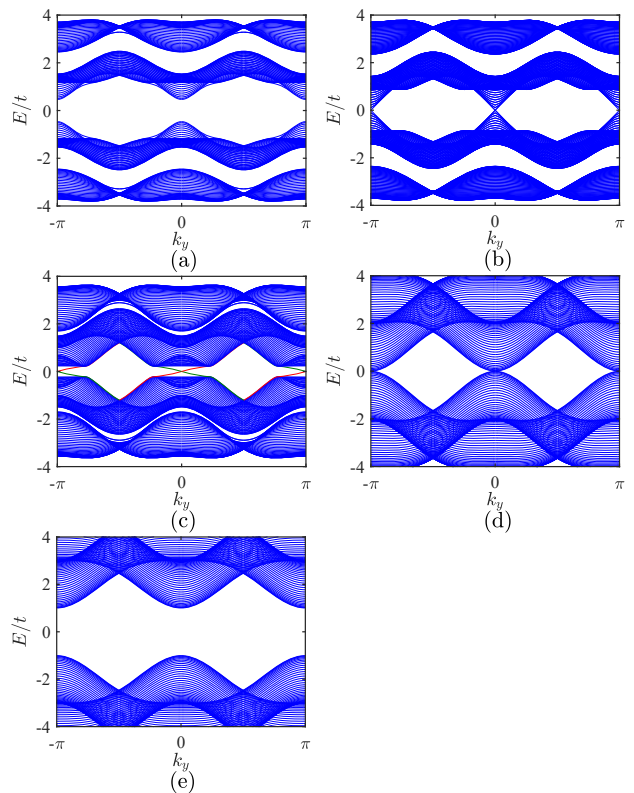


FIG. 2. The bulk and edge energy bands in Fig.1. (a) In the trivial SF, there is a quasi-particle gap due to the pairing. (b) Along h_{c1} , the bulk gap closes at the two gapless Dirac points at $(0, \pi)$ and $(\pi, 0)$. (c) In the $C = 2$ TSF, the bulk gap re-opens due to the pairing. However, in a sharp contrast to the trivial SF, there are also two gapless edge modes near $k_y = 0, \pi$ (re-drawn in Fig. 5). (d) Along h_{c2} , the bulk gap touches down quadratically at $(0, 0)$ and (π, π) . (e) In the BI, the bulk gap re-opens due to the Zeeman field. One may also view the band evolution by columns. In the first column, there are bulk gaps in (a) the trivial SF (c) the $C = 2$ SF (d) the BI. Only the $C = 2$ SF hosts two gapless edge states. In the second column, the bulk gap vanishes (b) at h_{c1} linearly at the two Dirac points at $(0, \pi)$ and $(\pi, 0)$, (d) at h_{c2} quadratically at $(0, 0)$ and (π, π) . There are two new classes of TPTs at h_{c1} and h_{c2} .

and (π, π) .

By introducing the superfluid order parameter Δ , one can perform the mean field calculations on the Hamiltonian Eq.1. By imposing the self-consistent equations, one can determine μ and Δ in terms of given N and (h, U) . In Sec.VII-A-1, we present the technical details in more general case with not only the nearest neighbour hopping t , but also the next nearest neighbour hopping t' in Eq.27. When applying the results listed in Sec.VII-A-1 to this section, one can simply set $t' = 0$ in Eq.29 and use Eqs.36,37, 38,39.

In this paper, we mainly focus on the half-filling case with $\mu = 0$. The effects of $\mu \neq 0$ will only be briefly discussed in Sec.VII. At the half filling with the chemical potential $\mu = 0$, the symmetry $E(\mathbf{k}) = E[(\pi, \pi) + \mathbf{k}]$ in

Eq.36 (with $t' = 0$) indicates the energies at the four momenta split into two groups $(0, 0)$, (π, π) and $(0, \pi)$, $(\pi, 0)$. At the extremely anisotropic limit ($\alpha = \pi/2, \beta$), the energies at the two groups become degenerate. Any deviation from the anisotropic limit splits the 4 degenerate minima into the two groups which opens a window for the TSF. The TSF window reaches maximum at the isotropic Rashba limit $\alpha = \beta$ where the symmetry is enlarged to $[C_4 \times C_4]_D$. The main results for $\mu = 0$ are shown in Fig.1.

One can understand some qualitative features near h_{c2} in Fig.1 starting from the non-interacting SOC fermion spectrum (namely the helicity basis) with no pairing $\Delta = 0$. At $h = 0$ axis in Fig.1, due to FS nesting, any $U < 0$ leads to a trivial SF. At $h_{c2} = 2t(\cos \alpha + \cos \beta)$, there is a quadratic band touching at $(0, 0)$ and (π, π) where there is already a gap $h - 2t(\cos \alpha - \cos \beta) = 4t \cos \beta$ opening at $(0, \pi)$ and $(\pi, 0)$. At $0 < h < h_{c2} = 2t(\cos \alpha + \cos \beta)$, due to the finite density of state (DOS) at the FS $\mu = 0$, a weak $U < 0$ leads to a TSF with the $p_x + ip_y$ pairing across 2 FS with the same helicity leading to $C = 2$. Here one gets a $C = 2$ TSF almost for free: at a small h and a small attractive interaction $U < 0$. At $h = h_{c2}$, the FS disappears, there is only quadratic band touching at $(0, 0)$ and (π, π) with a zero DOS, so one need a finite U_c to drive to a trivial SF. This explains why the $h = h_{c2}$ is a straight line ending at U_c at the M point in Fig.1. When $h > h_{c2}$, there is a band gap due to the Zeeman field at $\mu = 0$, so one need even a larger U_c to reach a SF. It turns out to be a 1st order transition to a trivial SF at h_b due to a jumping of the superfluid order parameter Δ , so it is a bosonic transition with gapped fermionic excitations on both sides of the transition. The first order transition may lead to a possible ‘‘phase separation’’ between the SF and BI in the two metastable regimes shown in Fig.1. Obviously, it is the SOC which leads to the multi-minima structure of the ground state energy landscape leading to the first order BI-SF transition. In fact, as shown in⁵⁷, the SOC also leads to multi-minima structure of magnon spectrum in spin-orbital correlated magnetic phases. So it is a generic feature for the SOC to lead to multi-minima structures in both the ground state and the excitation spectra.

Indeed, at $\mu = 0$, $\xi^2(\mathbf{k}_0)$ in Eq.39 split into two groups: $\xi^2(0, 0) = \xi^2(\pi, \pi) = 4t^2(\cos \alpha + \cos \beta)^2 > \xi^2(0, \pi) = \xi^2(\pi, 0) = 4t^2(\cos \alpha - \cos \beta)^2$. If neither α nor β equals to $\frac{\pi}{2}$, the two groups take two different values which divide the system into 3 different phases: SF, TSF and BI phase. At $h < h_{c1} = \sqrt{\xi^2(0, \pi) + \Delta^2}$, it is in a trivial SF phase where the fermionic excitation energy $E_{\mathbf{k}-}$ is gapped in the bulk with no edge states. There is a SF to TSF transition at h_{c1} where the $E_{\mathbf{k}-}$ touches zero linearly and simultaneously at the two Dirac points at $\mathbf{k} = (\pi, 0)$ and $(0, \pi)$ shown in Fig.1a. Then a second topological transition from the TSF to BI at $h_{c2} = |\xi(0, 0)| = |\xi(\pi, \pi)| = 2t(\cos \alpha + \cos \beta)$ where $\Delta = 0$ and the $E_{\mathbf{k}-}$ touches zero quadratically and simultaneously at $\mathbf{k} = (0, 0)$ and $(0, \pi)$ in Fig.1c. Inside

the TSF $h_{c1} < h < h_{c2}$, the bulk is gapped with two pairs of gapless edge states at $k_y = 0, \pi$ on the boundaries of a finite-size system in Fig.1b. In the BI $h > h_{c2}$, it has a bulk gap due to the Zeeman field in Fig.1d.

If either α or β is $\frac{\pi}{2}$ (assuming $\alpha = \frac{\pi}{2}$), the two groups take the same value $\xi^2(\mathbf{k}_0) = 4t^2 \cos^2 \beta = h_c^2$ which divides the system into only 2 different phases as shown in Fig.7. The TSF phase is squeezed to zero. At $h < h_c$, it is in the trivial SF phase with a bulk gap and no edge states. At $h = h_c$, the excitation energy $E_{\mathbf{k}-}$ touches zero quadratically and simultaneously at all four points shown in the inset of Fig.7. At $h > h_c$, it gets into the gapped BI phase.

The main text focus on the isotropic Rashba limit $\alpha = \beta$ where $\xi^2(0, \pi) = \xi^2(\pi, 0) = 0$. In the anisotropic limit $\alpha \neq \beta$, h_{c1} increases, the TSF phase shrinks (Fig.6). In the extremely anisotropic limit $\alpha = \pi/2$, $h_{c1} = h_{c2} = h_c$, the TSF phase shrinks to zero and disappears (Fig.7). They will be discussed in details in the appendix A and C respectively.

III. THE SF TO THE TSF TRANSITION AT $h = h_{c1}$.

In the bulk, the transition is driven by the gap closing of the two Dirac fermions at $(0, \pi)$ and $(\pi, 0)$ with the same chirality. Now we derive the effective 2×2 Hamiltonian $H(\vec{k})$ to describe the TPT near $h = h_{c1}$. At the $h_{c1} = \sqrt{\xi^2(0, \pi) + \Delta^2} = \Delta$ and at the two Dirac points $(0, \pi)$ and $(\pi, 0)$, following³¹, one can find a 4×4 unitary matrix $S_{(0, \pi)}$ to diagonalize the 4×4 Hamiltonian Eq.34: $S_{(0, \pi)}^\dagger H_{(0, \pi)} S_{(0, \pi)} = (2h_{c1}, -2h_{c1}, 0, 0)$. Now one can expand the Hamiltonian around h_{c1} and also near the Dirac point $(0, \pi)$ by writing $\delta h = h - h_{c1}$ and $\vec{k} = (0, \pi) + \vec{q}$, then separate the 4×4 Hamiltonian $\tilde{H} = S_{(0, \pi)}^\dagger H S_{(0, \pi)}$ into 2×2 blocks $\tilde{H} = \begin{bmatrix} H_H & H_C \\ H_C^\dagger & H_L \end{bmatrix}$ with the fermion field $\Phi(\mathbf{k}) = S_{(0, \pi)}^\dagger \Psi(\mathbf{k}) = (\phi_H, \phi_L)$. Projecting to the 2 component low energy spinor: $\phi_{L\mathbf{k}} = \frac{1}{\sqrt{2}} \begin{bmatrix} c_{-\mathbf{k}\uparrow}^\dagger - c_{\mathbf{k}\downarrow} \\ c_{-\mathbf{k}\downarrow}^\dagger - c_{\mathbf{k}\uparrow} \end{bmatrix}$ space, we find the effective Hamiltonian $H_{(0, \pi)} = H_L - H_C^\dagger H_H^{-1} H_C$:

$$H_{(0, \pi)} = \left(\delta h - \frac{t^2 \cos^2 \alpha (q_x^2 - q_y^2)^2}{2\Delta} \right) \sigma_3 + 2t \sin \alpha (q_x \sigma_1 + q_y \sigma_2) \quad (2)$$

where the Dirac fermion mass $M = \delta h = h - h_{c1}$ changes the sign across the TPT boundary $h = h_{c1}$. Note that because the SF order parameter Δ remains a constant across the TPT, so it is just a pure fermionic TPT inside the SF with the dynamic exponent $z = 1$.

Eq.2 can be cast into the form:

$$H(\vec{q}) = \epsilon(\vec{q}) + d_a(\vec{q})\sigma_a, \quad d_a(\vec{q}) = (Aq_x, Aq_y, M(\vec{q})) \quad (3)$$

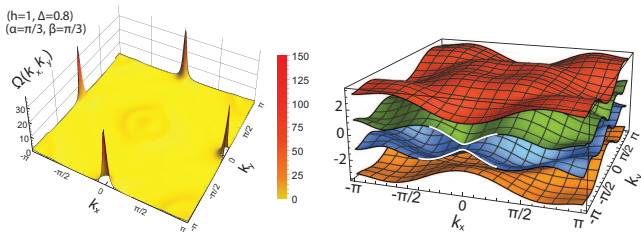


FIG. 3. (Color online) The Berry curvatures and energy bands at $[\alpha, \beta] = [\frac{\pi}{3}, \frac{\pi}{3}]$ near h_{c1} with $(h = 1, \Delta = 0.8)$ inside the TSF. (a) The Berry curvature is sharply peaked at $(0, \pi)$ and $(\pi, 0)$. (b) The four quasi-particle energy bands. The two middle bands have a minimum gap denoted by the wide lines which leads to the Berry curvature in (a) near $(0, \pi)$ and $(\pi, 0)$.

where $\epsilon(\vec{q}) = 0$ dictated by the P-H symmetry, $A = 2t \sin \alpha$ and $M(\vec{q}) = \delta h - B(q_x^2 - q_y^2)^2$ where $B = \frac{t^2 \cos^2 \alpha}{2\Delta} > 0$. The first Chern number is given by:

$$C_1 = \frac{1}{4\pi} \int dq_x dq_y \hat{\mathbf{d}} \cdot \left(\frac{\partial \hat{\mathbf{d}}}{\partial q_x} \times \frac{\partial \hat{\mathbf{d}}}{\partial q_y} \right) \quad (4)$$

where $\hat{\mathbf{d}}(\vec{q}) = \mathbf{d}(\vec{q})/|\mathbf{d}(\vec{q})|$ is a unit vector and the integral is over the 2d BZ in the original lattice model, but the whole 2d (k_x, k_y) plane in the continuum limit. In the TSF, $\delta h/B > 0$, $C_1 = 1$. In the trivial SF, $\delta h/B < 0$, $C_1 = 0$. The mass $M = \delta h$ changes sign at the TQCP and is the only relevant term. The $-B(q_x^2 - q_y^2)^2$ term is dangerous leading irrelevant near the TQCP in the sense that it is irrelevant at the TQCP, but it is important on the two sides of the TQCP and decide the thermal Hall conductivity of the two phases³⁵⁻³⁷.

Following the procedures in^{31,32}, we find the ground state energy shows a singularity at its third order derivative at the transition, so it is a 3rd order TPT.

One can get the effective Hamiltonian at $(\pi, 0)$ by changing $\sigma_1 \rightarrow -\sigma_1, \sigma_2 \rightarrow -\sigma_2$ in Eq.2 or equivalently $A \rightarrow -A$ in Eq.3, but still with the same ϕ_L , so the pairing remains the $p_x + ip_y$ form³³. Then Eq.4 shows $C_{(\pi,0)} = C_{(0,\pi)} = 1$, so the total Chern number $C = C_{(\pi,0)} + C_{(0,\pi)} = 2$. Of course, $H_{(0,\pi)}$ and $H_{(\pi,0)}$ are related by the $[C_4 \times C_4]_D$ symmetry at $\alpha = \beta$. In fact, the topological Chern number of a given band is the integral of the Berry curvature in the whole BZ shown in Eq.4. Here we show that the global topology can be evaluated just near a few isolated P-H symmetric points in an effective Hamiltonian in the continuum limit. Note that the topological Z_2 indices (Pfaffian) are also evaluated at some isolated symmetric points³⁰. They determine the topology of the bands in the whole BZ.

Using the original 4 bands theory and the three different methods outlined in the appendix C, we calculated the Berry Curvature of $E_-(\mathbf{q})$ in the whole BZ in Fig.3a and find that near h_{c1} , they are sharply peaked at $(0, \pi)$ and $(\pi, 0)$. The corresponding 4 energy bands are also shown in Fig.3a. These facts near $(0, \pi)$ and $(\pi, 0)$ can be precisely captured by the 2 bands effective theory Eq.2.

For example, from Eq.2, one can determine the energy of the two middle bands:

$$E_{\pm}(\mathbf{q}) = \pm \sqrt{\delta h^2 + 4t^2 \sin^2 \alpha (q_x^2 + q_y^2)} \quad (5)$$

which has a minimum at $\mathbf{q} = (0, 0)$ as shown in Fig.3b. It leads to the Berry curvature distribution near $(0, \pi)$ and $(\pi, 0)$ shown in Fig.3a.

IV. THE TSF TO THE BI TRANSITION AT $h = h_{c2}$

Near $h_{c2} = 2t(\cos \alpha + \cos \beta)$, there are quadratic band touching at $(0, 0)$ and (π, π) as shown in Fig.1c. Following similar procedures as those to derive the 2×2 effective Hamiltonian Eq.2 near h_{c1} and $(0, \pi)$, we derive the 2×2 effective Hamiltonian near h_{c2} and $(0, 0)$:

$$H_{(0,0)} = \left(\delta h - t \frac{1 + \cos^2 \alpha}{2 \cos \alpha} (q_x^2 + q_y^2) \right) \sigma_3 - \frac{\Delta \tan \alpha}{2} (q_x \sigma_1 + q_y \sigma_2) \quad (6)$$

where the two component low energy spinor $\phi_{L\mathbf{k}} = \frac{1}{\sqrt{2}} \begin{bmatrix} c_{-\mathbf{k}\downarrow}^\dagger \\ c_{\mathbf{k}\downarrow} \end{bmatrix}$ which contains only spin down. The Dirac fermion mass $M = \delta h = h_{c2} - h$ changes its sign across the TPT boundary $h = h_{c2}$.

Eq.6 can also be cast into the form Eq.3 where $\epsilon(\vec{k}) = 0$, $A = \frac{\Delta \tan \alpha}{2}$ and $M(\vec{k}) = \delta h - B(q_x^2 + q_y^2)$, $B = t \frac{1 + \cos^2 \alpha}{2 \cos \alpha} > 0$. The first Chern number is still given by Eq.4: If $M/B < 0$ and $\Delta = 0$ in the BI, $C_1 = 0$. It becomes a gapped non-relativistic fermion due to the Zeeman field: $E(k) \sim [h - h_{c2}] + B(q_x^2 + q_y^2)$. If $M/B > 0$ and $\Delta \neq 0$ in the TSF, $C_1 = 1$. There is also a gap opening due to the effective $p_x + ip_y$ pairing Δ . It has the dynamic exponent $z = 2$ at the QCP $\delta h = 0, \Delta = 0$. So there are two relevant operators: the mass term $M = \delta h$ and the $p_x + ip_y$ pairing term Δ . The $-B(q_x^2 + q_y^2)$ term is dangerous leading irrelevant near the QCP in the sense that it is irrelevant at the QCP, but it is important to the physical properties of the two phases on the two sides of the QCP.

One can get the effective Hamiltonian at (π, π) by changing $\sigma_1 \rightarrow -\sigma_1, \sigma_2 \rightarrow -\sigma_2$ in Eq.6 or equivalently $A \rightarrow -A$ in Eq.3. Especially, it has a different low energy two component spinor $\phi_{L\mathbf{k}} = \frac{1}{\sqrt{2}} \begin{bmatrix} c_{\mathbf{k}\uparrow} \\ c_{-\mathbf{k}\uparrow}^\dagger \end{bmatrix}$ which contains only spin up. Then Eq.4 shows $C_{(\pi,\pi)} = C_{(0,0)} = 1$, so the total Chern number $C = C_{(\pi,\pi)} + C_{(0,0)} = 2$ in the TSF. So the distribution of the Berry curvature is moving from $(0, \pi)$ and $(\pi, 0)$ near h_{c1} as shown in Fig.3a to $(0, 0)$ and (π, π) near h_{c2} shown in Fig.4a.

Indeed, using the original 4 bands theory, using three different methods (See appendix C), we calculated the Berry Curvature of $E_-(\mathbf{q})$ in the whole BZ in Fig.4a and find they are localized around $(0, 0)$ and (π, π) near h_{c2}

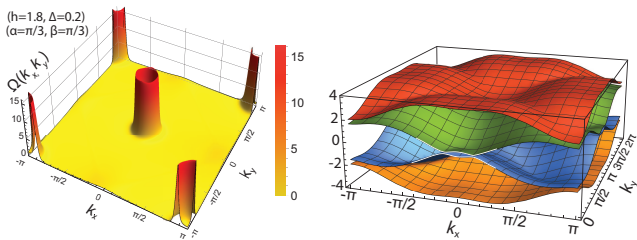


FIG. 4. (Color online) The Berry curvatures and energy bands at $[\alpha, \beta] = [\frac{\pi}{3}, \frac{\pi}{3}]$ near h_{c2} with $(h = 1.8, \Delta = 0.2)$ inside the TSF. (a) The Berry curvature has a dip at $(0, 0)$ and (π, π) , but peaked at a ring around the two Dirac points. (b) The four quasi-particle energy bands. The two middle bands have the shape denoted by the wide lines near $(0, 0)$ and (π, π) . The energy gap contour of the two middle bands are nearly circular which leads to the Berry curvature structure in (a). This bulk feature leads to the oscillating behavior of the edge state wavefunction when decaying into the bulk shown in Sec.V-B.

shown in Fig.4a. The corresponding 4 energy bands are also shown in Fig.4b. These facts can be precisely captured by the 2 bands effective theory Eq.6. For example, one can determine the bulk energy of the two middle bands:

$$E_{\pm}(\mathbf{q}) = \pm \sqrt{[M - B(q_x^2 + q_y^2)]^2 + A^2(q_x^2 + q_y^2)} \quad (7)$$

which means that in the TSF side $M = \delta h > 0$, if assuming $C = 2MB - A^2 > 0$, then it has a maximum at $\mathbf{q} = (0, 0)$ and a minimum at $q^2 = C/2B^2$ with a minimum gap $E_{min} = \frac{A\sqrt{4MB-A^2}}{2B} > 0$. This is indeed the case as shown in Fig.4b. It leads to the non-trivial Berry curvature distribution near $(0, 0)$ and (π, π) shown in Fig.4a. This non-trivial structure of the bulk gap is also crucial to explore the bulk-edge correspondence near h_{c2} in the next section.

The main difference between the TPT at $h = h_{c1}$ described by Eq.2 and that at h_{c2} described by Eq.6 is that in the former, the SF order parameter Δ is non-critical across the SF to TSF transition at h_{c1} , the effective $p_x + ip_y$ pairing amplitude in Eq.2 is given by the SOC strength $t \cos \alpha$, so it is a pure fermionic transition. However, in the latter, the SF order parameter Δ is also critical across the TSF to the BI transition at h_{c2} , the effective $p_x + ip_y$ pairing amplitude in Eq.2 is given by the S-wave pairing Δ multiplied by an SOC related factor $\tan \alpha$. So it involves two natures instead of just a pure fermionic transition: (1) Conventional bosonic nature due to the superfluid order parameter Δ . (2) Topological fermionic nature due to the Dirac fermions in the TSF side. It happens near the two Dirac points $(0, \pi)$ and $(\pi, 0)$ near h_{c1} in the Fig.1. However, it moves to $(0, 0)$ and (π, π) near h_{c2} .

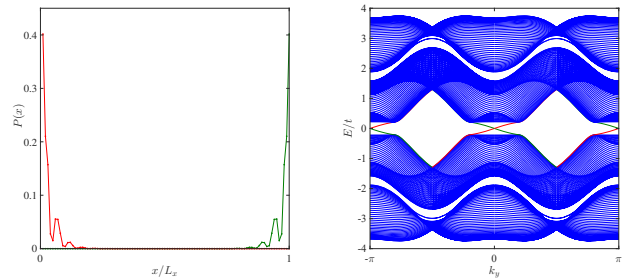


FIG. 5. (Color online) The normalized edge state wavefunction of the TSF in both real and momentum space at the two edges $x = 0, L$ and at $k_y = 0$. The SOC parameters are $[\alpha, \beta] = [\frac{\pi}{3}, \frac{\pi}{3}]$ and the (h, Δ) corresponding to one point inside the TSF near h_{c2} in Fig.1. (a) In the real space, it shows oscillating behaviors towards decaying into the bulk. The red and green lines show the two oppositely propagating edge modes on the two opposite sides of the sample. (b) In the momentum space, it show two edge states at $k_y = 0, \pi$. The red and green lines correspond to the edge mode in the left and right in (a) respectively.

V. EDGE MODES IN THE $C = 2$ TSF, OSCILLATION OF THE EDGE STATES AND BULK-EDGE CORRESPONDENCES.

As shown in Fig.1,5, using the open boundary conditions in the x directions, the Exact Diagonalization (ED) study near h_{c1} shows that in the TSF side with $C = 2$, there are two branches of Majorana fermion edge states $k_y = 0$ and $k_y = \pi$. In the trivial SF side with $C = 0$, there is no edge states. In the following, we analyze the two edge modes in the TSF from the effective actions Eq.2 near h_{c1} and Eq.6 near h_{c2} respectively.

A. Spin and spatial structures of the Edge states near h_{c1} .

As shown in Eq.2, the effective $p_x + ip_y$ pairing amplitude $\Delta_e = 2t \sin \alpha$ is relatively large, so the TSF has a relatively large gap. The notable feature near h_{c1} is that Eq.2 is not isotropic in (q_x, q_y) , so the edge state depends on orientation of the edge. Setting $\tilde{q}_x = (q_x - q_y)/\sqrt{2}$, $\tilde{q}_y = (q_x + q_y)/\sqrt{2}$, then making simultaneous rotation in the spin space, Eq.2 can be rewritten as:

$$\tilde{H}_{(0,\pi)} = \left(\delta h - \frac{t^2 \cos^2 \alpha \tilde{q}_x^2 \tilde{q}_y^2}{\Delta} \right) \sigma_3 + 2t \sin \alpha (\tilde{q}_x \tilde{\sigma}_1 + \tilde{q}_y \tilde{\sigma}_2) \quad (8)$$

So the edge state along the edge $\tilde{x} = 0$ (or $x = \pm y$) can be similarly constructed in the rotated $\tilde{\cdot}$ basis as in^{1,2}. However, to see the detailed structure of the edge state wavefunctions $u_{k_y}^*(x) = -v_{-k_y}(x)$ such as decaying into the bulk with possible oscillations, one may need keep higher order terms in the bulk effective action Eq.2.

In the expression of $\phi_{L\mathbf{k}}$ listed above Eq.2, k_y remain good quantum number, setting $k_x \rightarrow x$ leads to the edge operator at a given k_y :

$$c_{2L,k_y}(x) = \frac{1}{\sqrt{2}} \begin{bmatrix} c_{-k_y\uparrow}^\dagger(x) - c_{k_y\downarrow}(x) \\ c_{-k_y\downarrow}^\dagger(x) - c_{k_y\uparrow}(x) \end{bmatrix} \quad (9)$$

We get the Majorana edge mode $\gamma_2(k_y)$ in Eq.11:

$$\begin{aligned} \gamma_2(k_y) &= \frac{1}{\sqrt{2}} \int_0^\infty dx \left[\left(u_{k_y}^*(x) c_{-k_y\uparrow}^\dagger(x) - v_{k_y}^*(x) c_{k_y\uparrow}(x) \right) \right. \\ &\quad \left. + \left(v_{k_y}^*(x) c_{-k_y\downarrow}^\dagger(x) - u_{k_y}^*(x) c_{k_y\downarrow}(x) \right) \right] \\ &= \gamma_{2\uparrow}(k_y) + \gamma_{2\downarrow}(k_y) \end{aligned} \quad (10)$$

which satisfies $\gamma_2^\dagger(k_y) = \gamma_2(-k_y)$ and includes both spin up $\gamma_{2\uparrow}(k_y)$ in the first line and the spin down $\gamma_{2\downarrow}(k_y)$ in the second line.

Similarly, using the effective action $H_{(\pi,0)}$, one can derive the Majorana edge mode $\gamma_1(k_y)$ near $k_y = 0$ in Eq.11. Because the unitary transformation $S_{(\pi,0)} = S_{(0,\pi)}$, so the form of Eq.9 and Eq.10 hold also for $\gamma_1(k_y)$.

In terms of the Majorana edge mode γ_2 near $k_y = \pi$ in Eq.10 and γ_1 near $k_y = 0$, one can write the effective 1d Majorana fermion $\gamma_i^\dagger = \gamma_i, i = 1, 2$ edge Hamiltonian:

$$H_{edge} = \int dy [-iv_f \gamma_i \partial_y \gamma_i] \quad (11)$$

where $i = 1, 2$ stand for the two edge modes and $v_f = \Delta_e = 2t \sin \alpha$ is the edge velocity near h_{c1} .

The original edge Majorana fermion on the edge $x = 0$ can be expressed in terms of the two edge modes:

$$\psi_1(y) = \gamma_1(y) + (-1)^y \gamma_2(y) \quad (12)$$

where $\psi_1^\dagger(y) = \psi_1(y)$. So one can evaluate the Majorana fermion correlation functions along the 1d $x = 0$ edge Eq.11 and 12.

In fact, one can define another Majorana edge mode $\psi_2(y) = \gamma_1(y) + (-1)^{y+1} \gamma_2(y)$ which is decoupled, so plays no role. It is easy to check that for the two sets of Majorana fermions: $\{\gamma_i(y), \gamma_j(y')\} = \delta_{ij} \delta(y-y')$, $\gamma_i^\dagger(y) = \gamma_i(y)$, $\psi_i^\dagger(y) = \psi_i(y)$, $\{\psi_i(y), \psi_j(y')\} = 2\delta_{ij} \delta(y-y')$, $i, j = 1, 2$. The extra factor of 2 shows that the edge state contains 2 Majorana fermions³⁴.

B. The Spin and spatial structures of Edge states near h_{c2} .

As shown in Eq.6, the effective $p_x + ip_y$ pairing amplitude $\Delta_e = \Delta \tan \alpha / 2$ is relatively small, so the TSF has a relatively small gap. To get the edge modes along a edge at $x = 0$ near h_{c2} , we set $q_x \rightarrow -i\partial_x$ in Eq.6. Similar procedures as in² can be used to find the edge mode at a given k_y near h_{c2} by imposing the additional

Majorana fermion condition $u_{k_y}^*(x) = -v_{-k_y}(x)$. The $k_y = 0$ energy eigenvalue equation near h_{c1} is:

$$M + B\lambda^2 + A\lambda = 0 \quad (13)$$

where as written below Eq.6: $A = \frac{\Delta \tan \alpha}{2}$, $B = t \frac{1 + \cos^2 \alpha}{2 \cos \alpha}$, $M = \delta h$.

One salient feature here is that both A and M are critical near h_{c2} . By a simple GL analysis, $\Delta \sim (\delta h)^{1/2}$, so, in general, $D = A^2 - 4MB$ could be either positive or negative. However, as shown in Fig.4 and the main text, it is negative here, so Eq.13 has the two physical roots with negative real part:

$$\lambda_{3,4} = -\frac{A \pm i\sqrt{|D|}}{2B} \quad (14)$$

which we denote by $\lambda_3, \lambda_4 = \lambda_3^*$.

In a sharp contrast, near the TI to BI transition, M changes sign across the transition, so M is a small quantity, while A remains un-critical across the transition, so $D = A^2 - 4MB$ is always positive, the edge state wavefunctions decay into the bulk monotonically with no oscillations.

After imposing the additional hard boundary condition $\psi(x = 0) = 0$, we can find a unique $E = 0$ edge state wavefunction:

$$\begin{bmatrix} u_0(x) \\ v_0(x) \end{bmatrix} = iR \begin{bmatrix} -e^{i\frac{\pi}{4}} \\ e^{i\frac{\pi}{4}} \end{bmatrix} \left(e^{\lambda_3 x} - e^{\lambda_3^* x} \right) \quad (15)$$

where $R = \sqrt{\frac{|Re\lambda_3||\lambda_3|^2}{2(|Re\lambda_3|^2 + |\lambda_3|^2)}}$ is the normalization constant.

The magnitude of the wavefunction $|\Phi(x)|^2$ Eq.15 decays into the bulk with the decaying length $l_d^{-1} = |Re\lambda_3| = A/2B$ with oscillating period $l_o^{-1} = |Im\lambda_3| = \sqrt{|D|}/2B$ which is consistent with the decaying-oscillating behaviors in the ED study in Fig.5. Again, the above procedures can be extended to derive the wavefunction at any given k_y with the eigen-energy $E = v_f q_y$ where $v_f = A$. When comparing with the bulk energy spectrum Eq.7, we find that it is the oscillating length $l_o^{-1} = E_{min}/v_f$ which can be expressed as the minimum bulk gap over the edge velocity, while the decay length $l_d^{-1} = E_{min}/\sqrt{|D|}$ is more complicated than that near h_{c1} . Because $\sqrt{|D|} > A$, so $l_o < l_d$. These analytical predictions are indeed observed in the ED results in Fig.5. Fig.5a shows the wavefunction of the edge mode at a given k_y which was achieved by ED a $4L_x \times 4L_x$ matrix at any given k_y . Notably, the edge state wavefunction at a given k_y decay into the bulk with some oscillating behaviors.

In the expression of $\phi_{L\mathbf{k}}$ listed below Eq.6, setting $k_x \rightarrow x$ leads to the edge operator at a given k_y :

$$c_{3L,k_y}(x) = \begin{bmatrix} c_{-k_y\downarrow}^\dagger(x) \\ c_{k_y\downarrow}(x) \end{bmatrix} \quad (16)$$

which contains only spin down. The Majorana edge mode is given by:

$$\gamma_3(k_y) = \int dx \left[u_{k_y}^*(x) c_{-k_y\downarrow}^\dagger(x) + v_{k_y}^*(x) c_{k_y\downarrow}(x) \right] \quad (17)$$

which satisfies $\gamma_3^\dagger(k_y) = \gamma_3(-k_y)$ and includes the only spin down.

Similarly, using the effective action $H_{(\pi,\pi)}$, one find the Majorana fermion near $k_y = \pi$:

$$c_{4L,k_y}(x) = \begin{bmatrix} c_{k_y\uparrow}(x) \\ c_{-k_y\uparrow}^\dagger(x) \end{bmatrix} \quad (18)$$

which contains only spin up and

$$\gamma_4(k_y) = \int dx \left[u_{k_y}^*(x) c_{k_y\uparrow}(x) + v_{k_y}^*(x) c_{-k_y\uparrow}^\dagger(x) \right] \quad (19)$$

which satisfies $\gamma_4^\dagger(k_y) = \gamma_4(-k_y)$ and includes the only spin up.

In terms of the edge mode γ_3 near $k_y = 0$ in Eq.17 and γ_4 near $k_y = \pi$ in Eq.19, we also reach the same Eq.12 with $v_f = \Delta_e = \Delta \tan \alpha/2$, $i = 3, 4$ and $\psi_3(y) = \gamma_3(y) + (-1)^y \gamma_4(y)$. The crucial differences than the two Majorana fermions γ_1, γ_2 near h_{c1} is that γ_3 and γ_4 near h_{c2} contain only spin down and spin up respectively.

VI. MAJORANA BOUND STATES INSIDE A VORTEX CORE OF THE $C = 2$ TSF

It was known that at a $C = 1$ TSF, a $n = \pm 1$ vortex holds one Majorana fermion zero mode⁹. Here, we have a $C = 2$ TSF in Fig.1 with two chiral edge modes, In general, it is expected that the Chern number $C = 2$ is equal to the number of edge modes and also the number of Majorana zero modes inside a $n = \pm 1$ vortex core. Similar to the study of the edge states, one can use the effective action near h_{c1} and h_{c2} to study analytically the zero modes inside a S-wave vortex core. When introducing a vortex in the phase winding of the SF order parameter, it will affect most the low energy fermionic responses near $(0, \pi)$ and $(\pi, 0)$ when h is near h_{c1} or near $(0, 0)$ and (π, π) when h is near h_{c2} respectively. The existence and stability of the zero modes are protected by the Chern number Z class classification of the TSF, so are independent of the continuum approximation made in the effective actions. Similar continuum approximations were used to study the quasi-particles in the vortex states of high T_c superconductors³⁵⁻³⁷.

A. The spin structure of the two Majorana zero modes γ_1, γ_2 near h_{c1} :

In the 2×2 effective Hamiltonian Eq.2 near $(0, \pi)$ with $C = 1$, setting $\Delta \rightarrow \Delta_0 e^{i\theta}$, the first term remains intact, but the SOC strength in the second term $t \sin \alpha \rightarrow$

$t \sin \alpha e^{i\theta}$ acquires an effective phase from the order parameter phase winding. Setting $q_x \rightarrow -i\partial_x, q_y \rightarrow -i\partial_y$ and paying special attentions to the anisotropy in the $-B(q_x^2 - q_y^2)^2$ term, one may derive the wavefunctions $(u(\mathbf{r}), v(\mathbf{r}))$ satisfying $u^*(\mathbf{r}) = -v(\mathbf{r})$.

In the expression of $\phi_{L\mathbf{k}}$ listed above Eq.2, setting $\mathbf{k} \rightarrow \mathbf{r}$ leads to the particle operator at a given \mathbf{r} :

$$c_{2L}(\mathbf{r}) = \frac{1}{\sqrt{2}} \begin{bmatrix} c_{\uparrow}^\dagger(\mathbf{r}) - c_{\downarrow}(\mathbf{r}) \\ c_{\downarrow}^\dagger(\mathbf{r}) - c_{\uparrow}(\mathbf{r}) \end{bmatrix} \quad (20)$$

which contain both spin up and spin down. It can be fused with the zero-mode wavefunctions $(u(\mathbf{r}), v(\mathbf{r}))$ to lead to the Majorana zero mode γ_2 in Eq.22:

$$\begin{aligned} \gamma_2 &= \frac{1}{\sqrt{2}} \int d\mathbf{r} \left[\left(u^*(\mathbf{r}) c_{\uparrow}^\dagger(\mathbf{r}) - v^*(\mathbf{r}) c_{\uparrow}(\mathbf{r}) \right) \right. \\ &\quad \left. + \left(v^*(\mathbf{r}) c_{\downarrow}^\dagger(\mathbf{r}) - u^*(\mathbf{r}) c_{\downarrow}(\mathbf{r}) \right) \right] \\ &= \gamma_{2\uparrow} + \gamma_{2\downarrow} \end{aligned} \quad (21)$$

which satisfies $\gamma_2^\dagger = \gamma_2, \gamma_2^2 = 1/2$ and includes both spin up $\gamma_{2\uparrow}, \gamma_{2\uparrow}^2 = 1/4$ in the first line and the spin down $\gamma_{2\downarrow}, \gamma_{2\downarrow}^2 = 1/4$ in the second line.

One can do a similar calculation near $(\pi, 0)$ to get the second trapped Majorana zero mode γ_1 which also contains both spin up and spin down. One may combine the two trapped Majorana zero modes inside a S-wave vortex core near h_{c1} into a single Dirac fermion:

$$\psi_1 = \gamma_1 + i\gamma_2 \quad (22)$$

Its number $\psi_1^\dagger \psi_1 = 0, 1$ counts the occupations on the zero mode. Its exchange statistics is just a fermionic one. There is no long-range entanglement between two distant vortices. A local operation can change the Dirac fermion occupation number inside the vortex core.

B. The spin structure of the two Majorana zero modes γ_3, γ_4 near h_{c2} .

Similarly, in the 2×2 effective Hamiltonian Eq.6 near $(0, 0)$ with $C = 1$, setting $\Delta \rightarrow \Delta_0 e^{i\theta}$, the first term remains intact, the second term $\Delta \tan \alpha \rightarrow \Delta_0 \tan \alpha e^{i\theta}$ acquires the phase and is nothing but a $p_x + ip_y$ pairing vortex. The Majorana fermion zero mode inside such a cylindrical symmetric vortex core in the polar coordinate (r, θ) has been worked out in many previous literatures^{9,11-13,15}. Combining the known wavefunctions $(u(\mathbf{r}), v(\mathbf{r}))$ satisfying $u^*(\mathbf{r}) = -v(\mathbf{r})$ with

$$c_{3L}(\mathbf{r}) = \begin{bmatrix} c_{\downarrow}^\dagger(\mathbf{r}) \\ c_{\downarrow}(\mathbf{r}) \end{bmatrix} \quad (23)$$

leads to

$$\gamma_3 = \int d\mathbf{r} \left[u^*(\mathbf{r}) c_{\downarrow}^\dagger(\mathbf{r}) + v^*(\mathbf{r}) c_{\downarrow}(\mathbf{r}) \right] \quad (24)$$

which satisfies $\gamma_3^\dagger = \gamma_3, \gamma_3^2 = 1/2$ and includes the only spin down.

Similarly, using the effective action $H_{(\pi,\pi)}$, one can derive another Majorana zero mode γ_4 . Combining the known wavefunctions with

$$c_{4L}(\mathbf{r}) = \begin{bmatrix} c_\uparrow(\mathbf{r}) \\ c_\uparrow^\dagger(\mathbf{r}) \end{bmatrix} \quad (25)$$

lead to

$$\gamma_4 = \int d\mathbf{r} \left[u^*(\mathbf{r}) c_\uparrow(\mathbf{r}) + v^*(\mathbf{r}) c_\uparrow^\dagger(\mathbf{r}) \right] \quad (26)$$

which satisfies $\gamma_4^\dagger = \gamma_4, \gamma_4^2 = 1/2$ and includes the only spin up.

Combining the two trapped Majorana zero modes Eq.24 and Eq.26 inside a S-wave vortex core near h_{c2} leads to a single Dirac fermion $\psi_2 = \gamma_3 + i\gamma_4$.

It is instructive to compare Eq.12 with Eq.22 which leads to the following interesting edge-vortex core correspondence. In the former, the two Majorana edge modes are separated by the conserved momentum $k_y = \pi$ along the $x = 0$ edge, so their linear combination leads to the Majorana fermion ψ_1 with a twice magnitude. While, in the latter, the two Majorana edge modes are trapped inside the same vortex core, so can be combined into one Dirac fermion.

VII. COMPETITION BETWEEN SUPERFLUIDS AND THE CHARGE DENSITY WAVES

So far, we ignored the possible competitions between the SF and CDW. In this section, we will study such a competition. To be more complete, one may also add a diagonal hopping term in Eq.1:

$$H_D = -t' \sum_i \left[c_{i\sigma}^\dagger c_{i+\hat{x}+\hat{y},\sigma} + c_{i\sigma}^\dagger c_{i-\hat{x}+\hat{y},\sigma} + h.c. \right] \quad (27)$$

The symmetries of the Hamiltonian Eq.1 where $t' = 0$ were listed in Sec.II. With $t' \neq 0$ in Eq.27, the following symmetries remain: (1) $CH_{MF}(\mathbf{k})C^{-1} = -H_{MF}(-\mathbf{k})$, $\sigma_z H(\mathbf{k}) \sigma_z = H(-\mathbf{k})$. So it still picks up the four P-H invariant momenta $(0,0), (\pi,0), (0,\pi), (\pi,\pi)$. (2) the $[C_4 \times C_4]_D$ symmetry at the isotropic Rashba limit $\alpha = \beta$. It indicates the equivalence between $(0,\pi)$ and $(\pi,0)$.

However, the following two symmetries at $t' = 0$ are violated, because both must be accompanied by $t' \rightarrow -t'$. (a) the $E(\mathbf{k}) = E[(\pi,\pi) + \mathbf{k}]$ symmetry at the half filling with $\mu = 0$. It indicates the energies at the four momenta split into two groups $(0,0), (\pi,\pi)$ and $(0,\pi), (\pi,0)$. (b) the symmetries $\alpha \rightarrow \pi - \alpha, k_x \rightarrow \pi - k_x$ or $\beta \rightarrow \pi - \beta, k_y \rightarrow \pi - k_y$. At the extremely anisotropic limit ($\alpha = \pi/2, \beta$), it indicates the equivalence between $(0,0)$ and $(\pi,0)$, also between $(0,\pi)$ and (π,π) .

Combining the symmetries (a) and (b) at $t' = 0$ lead to the following facts: At the extremely anisotropic limit

($\alpha = \pi/2, \beta$), the energies at the two groups become degenerate. The TSF disappears. Any deviation from the anisotropic limit splits the 4 degenerate minima into the two groups which opens a window for the TSF. The TSF window reaches maximum at the isotropic Rashba limit $\alpha = \beta$ where the symmetry is enlarged to $[C_4 \times C_4]_D$.

Because $t' \neq 0$ violates both symmetries, so all these results do not hold anymore. So the structure of the phase diagram may change when $t' \neq 0$. In this section, we focus on the competition of the SF against the CDW in the presence of $t' \neq 0$ and leave the phase diagram of $t' \neq 0$ to a possible future publication.

A. The competition at mean field level in the weak coupling BCS limit

The kinetic term in Eq.1 plus the diagonal term in Eq.27 can be written as:

$$H_{0\mathbf{k}} = \xi_{\mathbf{k}} \left(c_{\mathbf{k}\uparrow}^\dagger c_{\mathbf{k}\uparrow} + c_{\mathbf{k}\downarrow}^\dagger c_{\mathbf{k}\downarrow} \right) - h \left(c_{\mathbf{k}\uparrow}^\dagger c_{\mathbf{k}\uparrow} - c_{\mathbf{k}\downarrow}^\dagger c_{\mathbf{k}\downarrow} \right) + \Lambda_{\mathbf{k}} c_{\mathbf{k}\downarrow}^\dagger c_{\mathbf{k}\uparrow} + h.c. \quad (28)$$

where

$$\xi_{\mathbf{k}} = -2t \left(\cos \alpha \cos k_x + \cos \beta \cos k_y + 2\frac{t'}{t} \cos k_x \cos k_y \right) - \mu$$

$$\Lambda_{\mathbf{k}} = 2t (\sin \alpha \sin k_x - i \sin \beta \sin k_y) \quad (29)$$

By treating SF and the (π,π) CDW instabilities on the equal footing, one can rewrite the on-site interacting term in Eq.1 as⁵³:

$$H_{int} = \frac{U}{L_x L_y} \left(\sum_{\mathbf{k}} c_{\mathbf{k}\uparrow}^\dagger c_{-\mathbf{k}\downarrow}^\dagger \right) \left(\sum_{\mathbf{k}'} c_{\mathbf{k}'\downarrow} c_{-\mathbf{k}'\uparrow} \right) + \frac{U}{L_x L_y} \left(\sum_{\mathbf{k}} c_{\mathbf{k}+\mathbf{Q}\uparrow}^\dagger c_{\mathbf{k}\uparrow}^\dagger \right) \left(\sum_{\mathbf{k}'} c_{\mathbf{k}'+\mathbf{Q}\downarrow}^\dagger c_{\mathbf{k}'\downarrow}^\dagger \right) = H_{SF} + H_{CDW} \quad (30)$$

where $\mathbf{Q} = [\pi, \pi]$, so $\mathbf{k} + \mathbf{Q} = \mathbf{k} - \mathbf{Q}$.

By introducing the SF order parameter Δ and the CDW ones G_σ , one can re-write Eq.30 as:

$$H_{int} = - \sum_{\mathbf{k}} \left(\Delta^* c_{\mathbf{k}\downarrow} c_{-\mathbf{k}\uparrow} + c_{\mathbf{k}\uparrow}^\dagger c_{-\mathbf{k}\downarrow}^\dagger \Delta \right) - \frac{L_x L_y}{U} |\Delta|^2 - \sum_{\mathbf{k}} \left[G_\uparrow c_{\mathbf{k}+\mathbf{Q}\downarrow}^\dagger c_{\mathbf{k}\downarrow} + G_\downarrow c_{\mathbf{k}+\mathbf{Q}\uparrow}^\dagger c_{\mathbf{k}\uparrow} \right] - \frac{L_x L_y}{U} G_\uparrow G_\downarrow \quad (31)$$

where the self-consistent equations lead to the SF order parameter and the CDW ones respectively:

$$\Delta = - \frac{U}{L_x L_y} \sum_{\mathbf{k}} \langle c_{\mathbf{k}\downarrow} c_{-\mathbf{k}\uparrow} \rangle$$

$$G_\sigma = - \frac{U}{L_x L_y} \sum_{\mathbf{k}} \langle c_{\mathbf{k}+\mathbf{Q}\sigma}^\dagger c_{\mathbf{k}\sigma} \rangle \quad (32)$$

It was known that with the Rashba SOC, there is no spin-polarization at any h , so one can set $G_\uparrow = G_\downarrow = \Delta_z$.

In fact, there is a more systematic way to treat SF and the CDW on the same footings. Here, for the interaction term, it is important to use the identity $(n_{i\uparrow} - 1/2)(n_{i\downarrow} - 1/2) = -\frac{2}{3}\vec{\eta}_i^2$ to explicitly keep the pseudo-spin $SU_{ps}(2)$ symmetry of the interaction term where $\eta^+ = c_{i\uparrow}^\dagger c_{i\downarrow}^\dagger, \eta^- = c_{i\downarrow} c_{i\uparrow}, \eta_z = \frac{1}{2}(-1)^i(n_i - 1)$ are the 3 pseudo-spin $SU_{ps}(2)$ generators. Only in this decoupling scheme, one can treat CDW and SF instabilities on the same footing. In fact, the competitions between the CDW and SF in the strong coupling limit Eqn.44 also implies such a democratic treatment is necessary at the weak coupling. Then one can introduce a unified SF + CDW order parameter $\vec{\Delta}_i$ to decouple the on-site $U < 0$ interaction:

$$\begin{aligned} H_{int} &= \frac{3}{8|U|} \sum_i \vec{\Delta}_i^2 + \sum_i \vec{\Delta}_i \cdot \vec{\eta}_{s,i} \\ &= \frac{3}{8|U|} \sum_i \left[\frac{|\Delta_+|^2 + |\Delta_-|^2}{2} + \Delta_z^2 \right] \\ &\quad + \sum_i \left[\frac{1}{2}(\Delta_+ \eta_s^- + \Delta_- \eta_s^+) + \Delta_z \eta_{sz} \right] \end{aligned} \quad (33)$$

$$H_{MF} = \sum_{\mathbf{k}} \left(\frac{1}{2} \begin{bmatrix} c_{\mathbf{k}\uparrow}^\dagger & c_{\mathbf{k}\downarrow}^\dagger & c_{-\mathbf{k}\uparrow} & c_{-\mathbf{k}\downarrow} \end{bmatrix} \begin{bmatrix} \xi_{\mathbf{k}} - h & \Lambda_{\mathbf{k}} & 0 & -\Delta \\ \Lambda_{\mathbf{k}}^\dagger & \xi_{\mathbf{k}} + h & \Delta & 0 \\ 0 & \Delta & -\xi_{\mathbf{k}} + h & \Lambda_{\mathbf{k}}^\dagger \\ -\Delta & 0 & \Lambda_{\mathbf{k}} & -\xi_{\mathbf{k}} - h \end{bmatrix} \begin{bmatrix} c_{\mathbf{k}\uparrow} \\ c_{\mathbf{k}\downarrow} \\ c_{-\mathbf{k}\uparrow}^\dagger \\ c_{-\mathbf{k}\downarrow}^\dagger \end{bmatrix} + \xi_{\mathbf{k}} \right) - \frac{\Delta^2}{U} \quad (34)$$

It can be diagonalized by introducing two sets of Bogoli-

where $\eta_s^+ = c_{i\uparrow}^\dagger c_{i\downarrow}^\dagger, \eta_s^- = c_{i\downarrow} c_{i\uparrow}, \eta_{sz} = \frac{1}{2}(-1)^i(n_i - 1)$ transform as the irreducible tensor of rank 1 under the pseudo-spin algebra $SU_{ps}(2)$. It is easy to see that for a SF, one may set $\Delta_+ = \Delta_- = \Delta$, Eq.33 is equivalent to Eq.30 and 31.

In the following, we discuss the SF and CDW respectively, then compare their ground state energies.

1. SF case .

Setting $\Delta_z = 0$ in Eq.31, one can rewrite the mean-field Hamiltonian in the Nambu representation:

ubov quasi-particles $\alpha_{\mathbf{k}\pm}$:

$$H_{MF} = \sum_{\mathbf{k}} \left[E_{\mathbf{k}+} \alpha_{\mathbf{k}+}^\dagger \alpha_{\mathbf{k}+} + E_{\mathbf{k}-} \alpha_{\mathbf{k}-}^\dagger \alpha_{\mathbf{k}-} \right] + E_G \quad (35)$$

where

Its quasi-particle excitation energies are:

$$E_{\mathbf{k}\pm} = \sqrt{\xi_{\mathbf{k}}^2 + |\Lambda_{\mathbf{k}}|^2 + h^2 + \Delta^2 \pm 2\sqrt{\xi_{\mathbf{k}}^2 [|\Lambda_{\mathbf{k}}|^2 + h^2] + h^2 \Delta^2}} \quad (36)$$

and its ground state energy is:

$$E_G = \sum_{\mathbf{k}} \left[\xi_{\mathbf{k}} - \frac{E_{\mathbf{k}+} + E_{\mathbf{k}-}}{2} \right] - \frac{\Delta^2}{U} \quad (37)$$

At zero temperature, given the experimentally controlled parameters U, h and N , one can determine the two

quantities Δ, μ by solving the self-consistent equations⁶⁰:

$$\begin{aligned} -\frac{\partial E_G}{\partial \mu} &= N \\ \frac{\partial E_G}{\partial \Delta} &= 0 \end{aligned} \quad (38)$$

It is easy to see that the lower branch $E_{\mathbf{k}-}$ in Eq.36 always has four extreme points at $(k_{0x}, k_{0y}) = (0, 0), (\pi, 0), (0, \pi),$ and (π, π) . If there exists any gapless fermionic excitation (i.e. $E_{\mathbf{k}-} = 0$), it must occur at

one or several of the four $\mathbf{k} = \mathbf{k}_0$ where $\Lambda_{\mathbf{k}_0} = 0$ and the Eq. 36 simplifies to:

$$E_{\mathbf{k}_0-} = \left| \sqrt{\xi_{\mathbf{k}_0}^2 + \Delta^2} - h \right| \quad (39)$$

which determines the possible TPT driven the gap closing of the fermionic excitations.

Now we focus on the half filling with the chemical potential $\mu = 0$ case. Using the $\mu = 0$ symmetries of the $E_{\mathbf{k}\pm}$ in Eq.36: $E(\mathbf{k}, t') = E[(\pi, \pi) + \mathbf{k}, -t']$, one can show

$$E_{\mathbf{k}\eta\eta'} = -\mu - 4t' \cos k_x \cos k_y + \eta \sqrt{\Delta_z^2 + h^2 + |\Lambda_{\mathbf{k}}|^2 + C_{\mathbf{k}}^2 + \eta' 2 \sqrt{C_{\mathbf{k}}^2 (h^2 + |\Lambda_{\mathbf{k}}|^2) + h^2 \Delta_z^2}}. \quad (40)$$

where $C_{\mathbf{k}} = -2t(\cos \alpha \cos k_x + \cos \beta \cos k_y)$.

The CDW Hamiltonian can be written as:

$$\begin{aligned} H &= \frac{1}{2} \sum_{\mathbf{k}, \eta, \eta'} E_{\mathbf{k}\eta\eta'} \alpha_{\mathbf{k}\eta\eta'}^\dagger \alpha_{\mathbf{k}\eta\eta'} - \frac{L_x L_y}{U} \Delta_z^2 \\ &= \frac{1}{2} \sum_{\mathbf{k}, \eta, \eta'} |E_{\mathbf{k}\eta\eta'}| \beta_{\mathbf{k}\eta\eta'}^\dagger \beta_{\mathbf{k}\eta\eta'} + E_G^{CDW} \end{aligned} \quad (41)$$

where $\beta_{\mathbf{k}\eta\eta'} = \alpha_{\mathbf{k}\eta\eta'} (E_{\mathbf{k}\eta\eta'} > 0) + \alpha_{\mathbf{k}\eta\eta'}^\dagger (E_{\mathbf{k}\eta\eta'} < 0)$ and the ground state energy is:

$$E_G^{CDW}(\Delta_z) = \frac{1}{4} \sum_{\mathbf{k}, \eta, \eta'} (E_{\mathbf{k}\eta\eta'} - |E_{\mathbf{k}\eta\eta'}|) - \frac{L_x L_y}{U} \Delta_z^2. \quad (42)$$

Using Eq.38 and the relation holding at $\mu = 0$:

$$E_G^{CDW}(-t') - E_G^{CDW}(t') = 8t' \sum_{\mathbf{k}} \cos k_x \cos k_y = 0 \quad (43)$$

One can show that $\mu = 0$ also implies the half filling $N = L_x L_y$ in the CDW.

3. The SF versus the CDW state

If $\mu = 0$ and $t' = 0$, because $\xi_{\mathbf{k}} = C_{\mathbf{k}}$ listed in Eq. and Eq.40 respectively, It is easy to see that the excitation spectra in the SF Eq.36 and those in the CDW Eq.40 are identical, so $E_G^{SF}(\Delta) = E_G^{CDW}(\Delta)$ at the BCS mean field level. To resolve the degeneracy, one must perform quantum fluctuations on both states to determine the true ground state. We expect the quantum fluctuations may favour the SF over the CDW state. This may also be interpreted as the weak coupling version of the ‘‘order from quantum disorder’’ phenomena⁶⁴.

However, for any $\mu \neq 0$ or $t' \neq 0$, $E_G^{SF}(\Delta) < E_G^{CDW}(\Delta)$. So any finite μ or t' favor SF over the CDW. As to be shown below, these results still hold in the strong coupling BEC limit. So we expect the results hold in the whole crossover from the BCS weak coupling limit to the BEC strong coupling limit.

that $\mu = 0$ implies the half-filling $N = L_x L_y$ (or $\nu = \frac{1}{2}$), So one only need to focus on the second self-consistent Equation in Eq.38 to determine the Δ . This substantially simplifies the determination of the ground state and phase transitions at any t, t' .

Eq.39's implications for $t' = 0$ case on topological fermionic phase transitions at h_{c1} and h_{c2} are presented in Sec.III and IV respectively.

2. CDW case

Setting $\Delta = 0$ in Eq.31, we find that there are also four excitation energies

B. The competition at the leading order in the strong coupling BEC limit

To perform strong coupling expansion when $U < 0$ and large in Eq.1 and 27, it is convenient to perform a particle-hole (PH) transformation $c_{i\uparrow} = \tilde{c}_{i\uparrow}, c_{i\downarrow} = \tilde{c}_{i\downarrow}^\dagger$ to transform $U < 0$ to $U > 0$ case. The spin flip terms due to the SOC in the kinetic term in Eqn.1 will be transformed to nearest neighbor pairing terms. The chemical potential μ and the Zeeman field h will exchange their roles. Then the strong coupling expansion developed at the positive $U \gg t$ case in^{29,65} can be applied here. To the order $t^2/U, t'^2/U$, after using the pseudo-spin to the hard core boson mapping⁶¹ $\tilde{S}_i^+ = c_{i\uparrow}^\dagger c_{i\downarrow}^\dagger = b_i^\dagger, \tilde{S}_i^- = c_{i\downarrow} c_{i\uparrow} = b_i, \tilde{S}_i^z = \frac{1}{2}(n_i - 1) = b_i^\dagger b_i - 1/2$, we find the effective Hamiltonian in the BEC limit:

$$\begin{aligned} H_b &= -J/2 \sum_{\langle i,j \rangle} (b_i^\dagger b_j + h.c.) + J \sum_{\langle i,j \rangle} (n_i^b - 1/2)(n_j^b - 1/2) \\ &\quad - J'/2 \sum_{\langle\langle i,j \rangle\rangle} (b_i^\dagger b_j + h.c.) + J' \sum_{\langle\langle i,j \rangle\rangle} (n_i^b - 1/2)(n_j^b - 1/2) \\ &\quad - \mu \sum_i (b_i^\dagger b_i - 1/2) \end{aligned} \quad (44)$$

where $J = 4t^2/U, J' = 4t'^2/U$. $\langle i, j \rangle$ and $\langle\langle i, j \rangle\rangle$ are NN and NNN bonds. There is no mixing term tt'/U at this order.

Unfortunately, in contrast to the RFHM^{29,57} in the $U \gg t$ case, the effects of SOC do not show up at this order. However, we do expect the effects of SOC will show up at the next order $t^2 t'/U^2$ which includes a ring exchange term around a triangle and t^4/U^3 which includes a ring exchange term around a square⁶⁵.

We first look at the square lattice by setting $t' = 0, \mu = 0$, then Eq.44 is nothing but the hard core boson at half filling hopping in a square lattice with the nearest neighbor interaction. It is at the $SU_{ps}(2)$ point where the SF and CDW are degenerate. So one must go to the next

order t^4/U^3 to determine the fate of the competition between SF and CDW. This may also be interpreted as the strong coupling version of the “order from quantum disorder” phenomena⁶⁴. However, any chemical potential $\mu \neq 0$ breaks the $SU_{ps}(2)$ symmetry and favors the SF order^{62,63}.

If setting $t' = 0$ in one diagonal bond, $t' = t$ in the other diagonal bond in Eq.27, then Eq.44 becomes the hard core boson at half filling hopping in a triangular lattice with the nearest neighbor interaction. It was known that in a triangular lattice, when $t/V_1 > 0.115$, it is in a SF state, otherwise, it will be in a supersolid state^{62,63}. Because in Eq.44, the nearest neighbour hopping $t = J/2$ and the nearest neighbour interaction $V_1 = J/2$, then $t/V_1 = 0.5 > 0.115$ in Eq.44, so it is always in the SF phase. In fact, as shown in the last subsection, we found that in the weak coupling BCS limit, the SF wins over the CDW also. So we expect that the system favors the SF in the whole BCS weak to BEC strong coupling regime.

In the general case with $t' \neq 0$ in both diagonal bonds, Eq.44 becomes a hard core boson at half filling hopping in a check-board lattice. It is always in the SF phase also. In fact, as shown in the last subsection, the SF wins over the CDW in the weak coupling also. So we expect that the system favors the SF in the whole crossover regime from the BCS weak coupling to BEC strong coupling.

C. Summary on the competition between the SF and the CDW

As shown in the two previous subsections, at half filling with the chemical potential $\mu = 0$, and also $t' = 0$, the SF and CDW are degenerate both at the mean field weak coupling BCS limit and in the leading order in the strong coupling BEC limit. Only quantum fluctuations in the weak coupling BCS limit can resolve the ground state energy differences between the SF and the CDW. In the conclusion section, we outline how to perform such quantum fluctuation calculations in the weak coupling BCS limit. We expect the quantum fluctuations may pick the SF state. In the strong coupling BEC limit, the SOC effects are absent in the leading order t^2/U the emergent $SU(2)_{sp}$ symmetry at this order dictates the degeneracy of the SF and the CDW at this order. However, the SOC effects will show up, $SU(2)_{sp}$ symmetry is explicitly broken to the next order t^4/U^3 including a ring exchange term around a square, so the degeneracy between the SF and the CDW must be broken. We expect the SOC may favor SF over the CDW due to the ring exchange term in the strong coupling BEC limit. It is important to perform some detailed calculations to confirm this expectation.

Moving away from the half-filling or adding the t' term, the $\mu = 0$ symmetry is lost. We showed that $\mu \neq 0$ or $t' \neq 0$ favors SF over CDW even at the mean field level in the weak coupling BCS theory, also in the strong coupling BEC limit even at the leading order in $t^2/U, t'^2/U$.

Due to the change of symmetries, the phase diagram with $\mu \neq 0$ or $t' \neq 0$ need to be determined again. For a general μ or t' , with a general SOC parameter α, β , the four $\xi_{\mathbf{k}_0}^2$ in Eq.39 could take four different values, so when tuning the Zeeman field through $h = \sqrt{\xi_{\mathbf{k}_0}^2 + \Delta^2}$ in Eq.39, one may drive the system to undergo four quantum or topological phase transitions into five phases, especially $C = \pm 1$ TSF. At $\alpha = \beta$, it reduces to 4 phases. All these new subjects will be addressed in a separate publication.

VIII. COMPARISON WITH PREVIOUS WORKS ON RELATED SYSTEMS

Obviously, the Hamiltonian Eq.1 and related systems have been studied in previous works with different focus. In this section, we will make critical comparisons between our results with those in these previous works.

It is constructive to compare the $C = 2$ TSF in Fig.1 with the 2d Time Reversal invariant TSF which is one copy of 2d $p_x + ip_y$ TSF with spin up plus its Time reversal partner of a 2d $p_x - ip_y$ with spin down (denoted as $(p_x + ip_y) \times (p_x - ip_y)$ in the class DIII in the 10 fold way classification)². In fact, after a unitary transformation, the surface of a 3d Topological insulator in the proximity of a S-wave superconductor also belongs to the same class DIII of 2d Time-reversal invariant TSF¹. Its two edge modes carry opposite spin and flow in opposite (chiral) direction. It is characterized by a Z_2 topological invariant. Here, the $C = 2$ TSF (belonging to the class D in the 10 fold way classification) breaks the Time reversal explicitly and has two copies of 2d $p_x + ip_y$ TSF related by the $\mu = 0$ symmetry. The two edge modes are separated by the momentum $k_y = \pi$, flow in the same (chiral) direction due to the explicit Time reversal symmetry breaking. It is characterized by a Z topological invariant. As shown in the Sec.V, the two edge modes carry similar spin structure near h_{c1} , but opposite one near h_{c2} .

The high Chern number $C = 2$ Topological superfluid was also identified numerically in⁶⁸. Now we make a critical comparison of this work with this earlier numerical work. Ref.⁶⁸ also found such a high Chern number $C = 2$ TSF, but did not make any analytical calculations to understand the physical properties of the $C = 2$ TSF, its neighboring phases and topological phase transitions between the $C = 2$ TSF and its neighboring phases. Specifically, there are at least the following crucial differences between the present work and Ref.⁶⁸: (1) In our global Phase diagram Fig.1, the $C = 2$ TSF is sandwiched by a trivial SF at h_{c1} and a band Insulator (BI) at $h = h_{c2}$. But the new phases BI is completely missing in this Ref. (2) Our manuscript investigated systematically the properties of the $C = 2$ TSF which are stressed in the title and the abstract. While the Ref. did not study the properties of the $C = 2$ TSF. (3) We found two novel classes of topological phase transitions

from the $C = 2$ TSF to its two neighboring phases at h_{c1} and h_{c2} described by the two novel effective actions in Eq.2 and Eq.6 respectively. The transitions are third order topological phase transitions. As stressed in the abstract, we used the two novel effective actions to examine all the novel properties of the $C = 2$ TSF. As pointed out in (1) above, Ref.⁶⁸ may not get the correct neighbouring phases around the $C = 2$ TSF, let alone to study the novel topological phase transitions from these neighbouring phases to the $C = 2$ TSF. (4) The two novel class of transitions at h_{c1} and h_{c2} motivated us to classify all the possible classes of topological phase transitions in a 2d square lattice which will be presented in a future publication (see the following section). In this future publication, we will incorporate the point group square lattice symmetry with the the Time reversal, parity and Chiral symmetry used in the 10 fold way classifications of the non-interacting topological phases. As said (3) above, the reference did not study any specific topological phase transitions, let alone inspire any clarifications of them. (5) We dedicate the whole Sec.VII to discuss the competition between the SF and CDW. This important competition was not even touched in⁶⁸.

There were previous studies on nearly zero modes inside a vortex core of a superconducting state in graphene^{66,67}. There are four of them. However, these four zero modes appear only in linear approximation, but are not protected by any topological indices, therefore can be lifted by lattice effects, in sharp contrast to the $C = 2$ Majorana zero modes here which are protected by the Z class of TSF.

IX. EXPERIMENTAL REALIZATION AND DETECTIONS.

At the half filling, the BI in Fig.1 only happens in a lattice. So the TSF to BI transition at h_{c2} in Fig.1 only happens in a lattice. The TSF happens in the regime with small h and small U in the Fig.1 which is the experimentally most easily accessible regime. This fact is very crucial for all the current cold atom experiments^{19-21,24,25,28} to probe possible many body effects of SOC fermion or spinor boson gases.

The topological order of the TSF does not survive up to any finite T . Of course, the BI does not survive up to any finite T either. There should be a KT transition above both the SF and TSF. The T_{KT} can be estimated as $T_{KT} \sim t \sim 3nK$ which is experimental reachable with the current cooling techniques^{38,39}. Using Eq.2 and following the procedures in^{31,32}, one may also write down the finite temperature scaling functions for several physical quantities such as specific heats, compressibility, Wilson ratio and thermal Hall conductivity³⁵ across the $T = 0$ SF to the $C = 2$ TSF transition near h_{c1} in Fig.1. Following the quantum impurity problems⁴⁰, one may also calculate the leading corrections to the scalings due to the leading dangerously irrelevant $-B(q_x^2 - q_y^2)^2$

operator. In fact, this term is irrelevant near the topological quantum critical point in the infra-red limit, but it controls the Ultra-Violet (UV) behaviours, leads to the Chern number $C = 2$ and also the global topological properties of the $C = 2$ TSF.

In cold atom systems loaded in an optical lattice, the effective Hamiltonian Eq.1 may be derived in a tight binding limit by projecting to the most relevant two pseudo-spin states. The effective parameters such as the hopping t , the SOC parameters (α, β) , and the onsite interaction U all depend on such a projection and can be estimated. However, the higher bands may also be relevant in the laser induced SOC lattice. A single particle (non-interacting $U = 0$) Rashba type of SOC in Eq.1 has been generated for the fermion ^{40}K gas^{19,20}, the Rashba type of SOC in Eq.1 with a many-body interaction $U \neq 0$ remain to be experimentally realized. Of course, as discussed in the introduction, various different experimental schemes²²⁻²⁸ are being implemented to realize such a Rashba type of SOC Hamiltonian with a many-body interaction U . A closely related (but different) QAH type of SOC for ^{87}Rb atoms has been experimentally implemented in²¹.

Now we discuss the experimental detections of Fig.1 in the cold atom systems. The fermionic quasi-particle spectrum can be detected by photoemission spectroscopy⁴¹. The topological phase transitions and the BCS to BEC crossovers in Fig.1 can also be monitored by the radio-frequency dissociation spectra^{42,47}. The energy gaps of the two middle bands in Fig.3b and Fig.4b can be detected by the momentum resolved inter-band transitions⁴³. The bulk $C = 2$ Chern numbers can be measured by the techniques developed in⁴⁴. The edge states can be directly imaged through Time of flight kind of measurements⁴⁵. A vortex can be generated by rotating the harmonic trap⁷⁰. The Majorana zero modes and the associated spin and spatial structures inside the vortex core can be imaged through In Situ measurements⁴⁶.

X. CONCLUSIONS AND DISCUSSIONS

Fig.1 shows that at any value of Zeeman field, both the TSF and trivial SF are fully gapped, there is no fermions left unpaired. This is another salient feature due to the SOC which favors SF phase in a Zeeman field. It is the SOC which splits the FS leading to complete pairings even in a Zeeman field. This is in sharp contrast to S-wave pairing of spin-imbalanced fermions without SOC due to a Zeeman field where there are always fermions left unpaired⁴⁸⁻⁵⁰. The absence of FFLO state of SOC fermions with a negative interaction in a Zeeman field reflects well the absence of Ferromagnetic state of SOC fermions with a repulsive interaction^{51,52}.

In Ref.⁵⁸, we studied the same model Eq.1 with the repulsive interaction $U > 0$ at a zero Zeeman field $h = 0$. The positive interaction leads to spin-bond correlated magnetic phases. Along the extremely anisotropic line

($\alpha = \pi/2, \beta$), the ground state remains the $Y - (0, \pi)$ state along the whole line and also from the weak to strong coupling. There is a only a crossover from the weak coupling to the strong coupling along this line. However, along the diagonal line $\alpha = \beta$, there must be some quantum phase transitions from the $X - (\pi, \pi)$ or $Y - (\pi, \pi)$ spin-bond correlated magnetic state at weak coupling to some other spin-bond correlated magnetic states in the strong coupling⁵⁹. The effects of a Zeeman field in the strong repulsively interacting limit was studied in^{56,57}. Due to the lack of the spin $SU(2)$ symmetry, different orientations of the Zeeman field lead to different phenomena^{56,57}. In this paper, we only focused on the normal Zeeman field, it may be also interesting to study the effects of in-plane fields in Eq.1.

The multi-minima structure in the ground states in Fig.1 is responsible to the 1st order transition between the BI and the SF, also the topological first order transition from the SF and the TSF between the T and M point in Fig.1. It was shown in⁵⁹ that the potential second order transition driven by the condensations of magnons in the Y-x state is pre-empted by a first order transition between Y-x state and an In-commensurate co-planar phase in the Rotated Heisenberg model in the generic (α, β) phase diagram. These first order transitions lead to associated phase separations, meta-stable phases and hysteresis. In fact, the multi-minima structure also exists in the in-commensurate magnons above a commensurate ground state⁵⁷. It is the SOC which lead to all these salient features in different contexts.

Going beyond the BCS mean field level, it maybe important to incorporate the quantum fluctuation effects. By writing the pairing $\Delta = \sqrt{\Delta_0 + \delta\rho}e^{i\theta}$, at the half filling $\mu = 0$, we expect there exists both gapless Goldstone mode θ and stable gapped Higgs mode $\delta\rho$ as the collective excitation⁵⁴ inside both the TSF and trial SF. Near h_{c1} in Eq.2, it is important to study the coupling between the Goldstone mode, also the Higgs mode and the gapless Dirac fermions at $(0, \pi)$ and $(\pi, 0)$ to investigate how the gapless Goldstone mode changes the universality class of the TPT at h_{c1} , also the decay rate of the Higgs mode. Near h_{c2} in Eq.6, following the methods developed in^{35,55}, it is interesting to construct a Ginsburg Landau action to perform a Renormalization group analysis. This action will include the bosonic sector for the superfluid order parameter $\Phi(\mathbf{r})$, the fermionic sector $\psi(\mathbf{r})$ at $(0, 0)$ and (π, π) for the topological order and an effective $p_x + ip_y$ coupling between the two sectors. Between h_{c1} and h_{c2} , the $C = 2$ TSF has a fermionic gap in the bulk, but two gapless modes Eq.11, it maybe interesting to study how does the bulk gapless Goldstone mode interact with the two gapless edge modes.

In this work, we constructed the effective actions to study the two new classes of topological phase transitions in the class D ($p_x + ip_y$ TSF) at a 2d square lattice. Obviously, the underlying 2d square lattice plays crucial roles for the existence of the trivial SF, $C = 2$ TSF, the BI and the two TPTs between the three phases. In a future pub-

lication, we will construct effective actions to describe all the TPT at a 2d square lattice: namely, those in the class A (Quantum Anomalous Hall) and Class C ($d + id$ TSF) which can be described by the Chern number Z and $2Z$ respectively, also the corresponding Time-reversal partners of class A and D: the class AII (Topological insulator) and class DIII ($(p_x + ip_y) \times (p_x - ip_y)$ TSF) which can be described by a Z_2 topological number. Obviously, the 10 fold way classifications only focus on the two non-spatial symmetries such as the Time reversal and the P-H symmetry with the chiral symmetry as the product of the two, while ignoring the spatial lattice symmetries. Any classifications of the TPTs may need to also consider the point group (which is the $[C_4 \times C_4]_D$ symmetry in the present 2d square lattice case) symmetries of the underlying lattice. It may also be interesting to extend these actions at a 2d square lattice to other lattices at 2d, then to all the non-trivial cases in the other 9 dimensions in suitable lattices in the 10 fold way classifications by dimensional shifts.

Acknowledgements

J. Ye thank X. L. Qi for helpful discussions during his visit at KITP. We thank W.-M. Liu for encouragements. J. Ye and F. Sun are supported by AFOSR FA9550-16-1-0412. Yu Y.-X. is supported by the NKRDP of China under grants No. 2016YFA0301500, NSFC under grants Nos. 11434015, 61227902, 61835013, and SPRPCAS under grants No. XDB01020300, XDB21030300. The work at KITP was supported by NSF PHY11-25915.

Appendix A: The general case with $\alpha \neq \beta$

The 2d SOC parameter (α, β) are experimentally tunable. When moving away from the isotropic limit $\beta < \alpha$, the $[C_4 \times C_4]_D$ symmetry is absent, the h_{c1} increases to:

$$h_{c1} = \sqrt{h_0^2 + \Delta^2} \quad (\text{A1})$$

where $h_0^2 = \xi^2(0, \pi) = \xi^2(\pi, 0) = 4t^2(\cos\alpha - \cos\beta)^2$. It vanishes in the isotropic limit $\alpha = \beta$ as discussed in the main text. While $h_{c2} = 2t(\cos\alpha + \cos\beta)$.

The phase diagram for ($\alpha = \pi/3, \beta = \pi/6$) is shown in Fig.6 where the TSF phase regime shrinks. Following the same procedures as those at $\alpha = \beta$, one can derive an effective action near h_{c1} and near the momentum $(0, \pi)$ or $(\pi, 0)$. However, due to the lack of the $[C_4 \times C_4]_D$ symmetry at any $\alpha \neq \beta$, the effective action looks more complicated than Eq.2, but it is in the same universality class with a different local distribution of the Berry curvature than in Fig.2a. Similar statements can be made on the effective action near h_{c2} and near the momentum $(0, 0)$ or (π, π) .

Note that despite the lack of $[C_4 \times C_4]_D$ symmetry at any $\alpha \neq \beta$, the $\mu = 0$ symmetries remain which indicate the equivalence between the effective action at $(0, \pi)$ and that at $(\pi, 0)$, between the effective action at $(0, 0)$

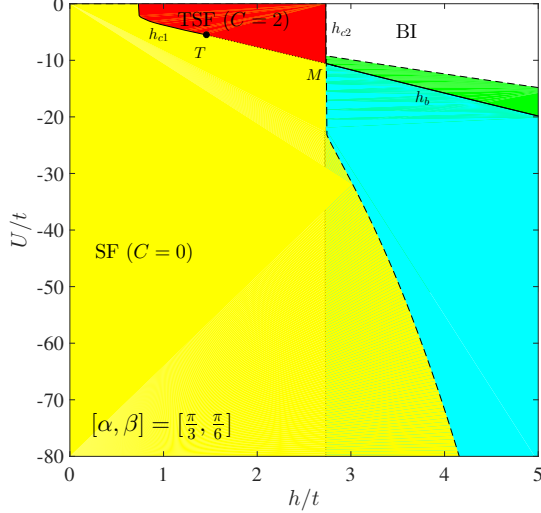


FIG. 6. (Color online) The global phase diagram in the parameter space of U and h at $[\alpha, \beta] = [\frac{\pi}{3}, \frac{\pi}{6}]$. The TSF regime starts to appear and the h_{c1} starts to approach to h_{c2} . Compare to Fig.1.

and that at (π, π) after suitable unitary transformations. Specific calculations showed that this is indeed the case.

Appendix B: The extremely anisotropic limit at $(\alpha = \pi/2, \beta)$.

It was found that in the absence of the Zeeman field, there is a spin-orbital coupled $U(1)_{soc}$ symmetry²⁹ along the anisotropic limit at $(\alpha = \pi/2, \beta)$. The $U(1)_{soc}$ symmetry is kept when the Zeeman field is along the \hat{y} axis⁵⁶. However, it was broken when the Zeeman field is along the \hat{x} axis or the \hat{z} axis⁵⁷. Similarly, the Zeeman field along the \hat{z} axis in Eq.1 also breaks the $U(1)_{soc}$. However, as said in Sec.II, the symmetry $\alpha \rightarrow \pi - \alpha, k_x \rightarrow \pi - k_x$ indicates the equivalence between $(0, 0)$ and $(\pi, 0)$, also between $(0, \pi)$ and (π, π) at $\alpha = \pi/2$. Then the two critical fields become the same $h_{c1} = h_{c2} = h_c = 2t \cos \beta$. The global phase diagram is shown in Fig.7 where there are only two phases SF and NI, the TSF phase is squeezed out.

The quasi-particle energy at the four points $(0, 0)$, (π, π) and $(0, \pi)$, $(\pi, 0)$ all touch zero quadratically at the same time. Following the similar procedures to derive Eq.2 and Eq.6, we reach the effective actions near the 4 points:

$$H_{h_c} = \pm \left[\delta h + \frac{\Delta^2}{4t \cos \beta} - \frac{t}{\cos \beta} (q_x^2 + q_y^2) \right] \sigma_3 \pm \frac{\Delta}{\cos \beta} (q_x \sigma_1 + \sin \beta q_y \sigma_2) \quad (B1)$$

where $\delta h = h_c - h$ and $(+, -)$, $(+, +)$ and $(-, +)$, $(-, -)$ are for $(0, 0)$, (π, π) and $(0, \pi)$, $(\pi, 0)$ respectively. When

$\delta h > 0$ and $\Delta \neq 0$, it is in the SF phase. When $\delta h < 0$ and $\Delta = 0$, it is in the BI phase.

In the SF side, $\delta h > 0$ and $\Delta \neq 0$, Eq.B1 near any of the four points can also be cast into the form Eq.6 where $\epsilon(\vec{k}) = 0$ and $M(\vec{k}) = M - B(q_x^2 + q_y^2)$, $M = \delta h + \frac{\Delta^2}{4t \cos \beta}$, $B > 0$. The first Chern number is still given by Eq.4: If $M/B > 0$ and $\Delta \neq 0$ in the SF, $C_1 = \pm 1$. If $M/B < 0$ and $\Delta = 0$ in the BI, $C_1 = 0$. However, the two gapped Dirac fermions at $(0, \pi)$, $(\pi, 0)$ carry the same topological charges⁵⁸ $\mu = 1$, so leading to the Chern number $C_{\mu=1} = C_{(0,\pi)} + C_{(\pi,0)} = 2$. While the two gapped Dirac fermions at $(0, 0)$, (π, π) carry opposite topological charges⁵⁸ $\mu = -1$, so leading to the Chern number $C_{\mu=-1} = C_{(0,0)} + C_{(\pi,\pi)} = -2$. So the total Chern number is $C = 2 - 2 = 0$, it is a trivial SF. It indicates the 4 gapped Dirac fermions can annihilate without going through a phase transition.

In fact, as stressed in Sec.IV and V, the topological Chern number of a given band is the integral of the Berry curvature in the whole BZ shown in Eq.C2. Here we show that the global topology can be evaluated just near a few isolated points in an effective Hamiltonian in a continuum limit. If looking at the 4 points separately, it seems there is topological transition from a BI to a TSF with $C = \pm 1$. However, the total Chern number $C = 1 + 1 - 1 - 1 = 0$, so globally it is still a BI to a trivial SF transition shown in Fig.7.

Using the original 4 bands theory, using three different methods outlined in Sec.IV, we calculated the Berry Curvature of $E_-(\mathbf{q})$ in the whole BZ in Fig.8a and find they are localized around $(0, 0)$, (π, π) and $(0, \pi)$, $(\pi, 0)$ respectively with $C = 1, 1, -1, -1$. The corresponding 4 energy bands are also calculated (but not shown). We only draw the energy gap contour of the two middle bands E_{k-} in Fig.8b which leads to the non-trivial Berry curvature structure shown in Fig.8a. All these facts can be precisely captured by the 2 bands effective theory Eq.B1.

Appendix C: The bulk Chern number calculations in the original 4 bands

In the main text, after deriving the effective 2 band theory, we used Eq.4 to calculate the first Chern number of a phase. In the following, we use 3 different methods to calculate the Berry curvature in the original 4 bands on the square lattice. The results are shown in Fig.2,3 and 8. We solve the eigenvalue problem (numerically) $H_k |\psi_{nk}\rangle = \omega_n |\psi_{nk}\rangle$ where the H_k is given in Eq.34 and the eigen-energies $\omega_1 = -E_{k+}$, $\omega_2 = -E_{k-}$, $\omega_3 = E_{k-}$, $\omega_4 = E_{k+}$.

1. *Method 1:* The Berry curvature for a given band is

$$\Omega_n(\mathbf{k}) = i[(\partial_x \psi_{nk}^*) (\partial_y \psi_{nk}) - (\partial_y \psi_{nk}^*) (\partial_x \psi_{nk})] \quad (C1)$$

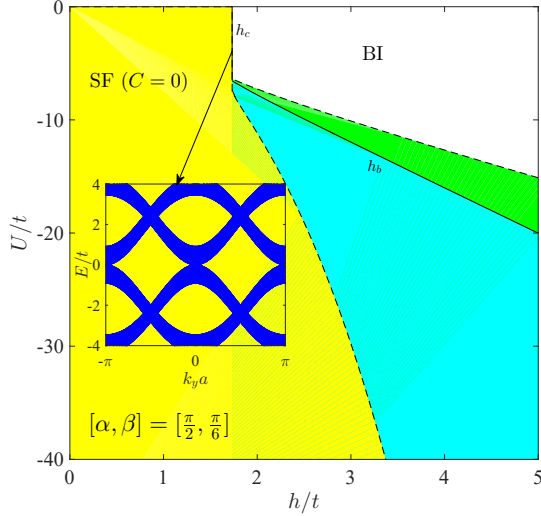


FIG. 7. (Color online) The global phase diagram in the parameter space of U and h at $[\alpha, \beta] = [\frac{\pi}{2}, \frac{\pi}{6}]$. The TSF regime shrinks to zero due to $h_{c1} = h_{c2} = h_c$. Inset: the quadratic band touching at the 4 Dirac points.

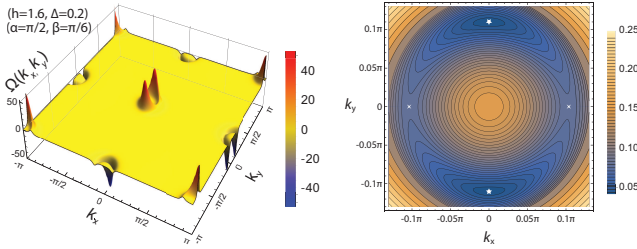


FIG. 8. (Color online) The Berry curvatures and energy bands at $[\alpha, \beta] = [\frac{\pi}{2}, \frac{\pi}{6}]$ near h_c with $(h = 1, \Delta = 0.8)$ inside the SF. (a) The Berry curvature has two split peaks along k_y axis around $(0, 0), (\pi, \pi)$ with local $C = 1$ and $(0, \pi), (\pi, 0)$ with local $C = -1$. Despite the local non-vanishing Chern numbers, the total $C = 0$. (b) The energy gap contour of the two middle bands E_{k-} have two minima denoted by two stars along the k_y axis and two saddle points denoted by the two crosses along the k_x axis. This gap structure leads to that of the Berry curvature in (a).

We numerically evaluate the Chern number by an integration over the whole BZ:

$$C_n = \frac{1}{2\pi} \int_{\text{BZ}} d^2k \Omega_n(k) \quad (\text{C2})$$

Using the default numerical integration method, we obtained $C_2 = 1.9999999887582889 = 2$ when $[\alpha, \beta] = [\pi/3, \pi/3]$ and $(h, \Delta) = (1, 1/2)$ falling inside the TSF in Fig.1.

2. *Method 2:* Eq.C1 can also be written as

$$\Omega_n(k) = - \sum_{n' \neq n} \frac{2\text{Im}\langle \psi_{nk} | (\partial_x H_k) | \psi_{n'k} \rangle \langle \psi_{n'k} | (\partial_y H_k) | \psi_{nk} \rangle}{(\omega_{n'} - \omega_n)^2} \quad (\text{C3})$$

Setting $[\alpha, \beta] = [\pi/3, \pi/3]$. When $(h, \Delta) = (1, 1/2)$ falling in the TSF, $C_1 = -1.63415 \times 10^{-12} = 0$, $C_2 = 2.000000000001559 = 2$.

When $(h, \Delta) = (1, 2)$ falling in the SF, $C_1 = 2.15106 \times 10^{-16} = 0$, $C_2 = 5.99347 \times 10^{-16} = 0$.

When $(h, \Delta) = (4, 1/2)$ falling in the BI, $C_1 = 3.06829 \times 10^{-16} = 0$, $C_2 = -2.31586 \times 10^{-16} = 0$.

2. *Method 3:* This method was designed in⁶⁹ to give exact integer Chern numbers. One first define a $U(1)$ link variable from the wave functions of the n -th band as:

$$U_\mu(k_l) = \langle \psi_n(k_l) | \psi_n(k_l + \hat{\mu}_i) \rangle / \langle \psi_n(k_l) | \psi_n(k_l + \hat{\mu}) \rangle \quad (\text{C4})$$

where $\hat{\mu}_i$ is a vector in the direction $i = x, y$ with the magnitude $2\pi/N_i$. Then one define a lattice field strength as,

$$F_{xy}(k_l) = \ln[U_x(k_l)U_y(k_l + \mu_x)U_x(k_l + \mu_y)^{-1}U_y(k_l)^{-1}] \quad (\text{C5})$$

where the principal branch of the logarithm is with, $-\pi < F_{xy}/i \leq \pi$. The Chern number associated to the band ω_n is given by,

$$C_n = \frac{i}{2\pi} \sum_l F_{xy}(k_l) \quad (\text{C6})$$

It is a very efficient method. Within 10 seconds on a conventional laptop, we obtain $C_1 = 0$, $C_2 = 2$, $C_3 = -2$ and $C_4 = 0$ when $(h, \Delta) = (1, 1/2)$ falling in the TSF.

We also used the three methods to calculate the Berry curvature using the 2 bands effective actions in Eq.2,6 and Eq.B1 and found they reproduce those from the original four bands theory shown in Fig.2, 3 and 8 very precisely.

¹ M. Z. Hasan and C. L. Kane, Colloquium: Topological insulators, Rev. Mod. Phys. **82**, 3045 (2010).

² X. L. Qi and S. C. Zhang, Topological insulators and superconductors, Rev. Mod. Phys. **83**, 1057 (2011).

³ A. M. Turner and A. Vishwanath, Beyond band insulators:

Topology of semi-metals and interacting phases, arXiv: 1301.0330.

⁴ S.-Y. Xu, N. Alidoust, I. Belopolski, Z. Yuan, G. Bian, T.-R. Chang, H. Zheng, V. N. Strocov, D. S. Sanchez, G. Chang, C. Zhang, D. Mou, Y. Wu, L. Huang, C.-C. Lee,

- S.-M. Huang, B. Wang, A. Bansil, H.-T. Jeng, T. Neupert, A. Kaminski, H. Lin, S. Jia, and M. Z. Hasan, Discovery of a Weyl fermion state with Fermi arcs in niobium arsenide, *Nat. Phys.* **11**, 748 (2015).
- ⁵ S.-Y. Xu, I. Belopolski, N. Alidoust, M. Neupane, G. Bian, C. Zhang, R. Sankar, G. Chang, Z. Yuan, C.-C. Lee, S.-M. Huang, H. Zheng, J. Ma, D. S. Sanchez, B. Wang, A. Bansil, F. Chou, P. P. Shibayev, H. Lin, S. Jia, and M. Z. Hasan, Discovery of a Weyl fermion semimetal and topological Fermi arcs, *Science* **349**, 613 (2015).
- ⁶ L. X. Yang, Z. K. Liu, Y. Sun, H. Peng, H. F. Yang, T. Zhang, B. Zhou, Y. Zhang, Y. F. Guo, M. Rahn, D. Prabhakaran, Z. Hussain, S.-K. Mo, C. Felser, B. Yan, and Y. L. Chen, Weyl semimetal phase in the non-centrosymmetric compound TaAs, *Nat. Phys.* **11**, 728 (2015).
- ⁷ B. Q. Lv, N. Xu, H. M. Weng, J. Z. Ma, P. Richard, X. C. Huang, L. X. Zhao, G. F. Chen, C. Matt, F. Bisti, V. Stokov, J. Mesot, Z. Fang, X. Dai, T. Qian, M. Shi, and H. Ding, Observation of Weyl nodes in TaAs, *Nat. Phys.* **11**, 724 (2015).
- ⁸ L. Lu, Z. Wang, D. Ye, L. Ran, L. Fu, J. D. Joannopoulos, and M. Soljačić, Experimental observation of Weyl points, *Science* **349**, 622 (2015).
- ⁹ N. Read and D. Green, Paired states of fermions in two dimensions with breaking of parity and time-reversal symmetries and the fractional quantum Hall effect, *Phys. Rev. B* **61**, 10267 (2000).
- ¹⁰ I. Bloch, J. Dalibard, and W. Zwerger, Many-body physics with ultracold gases, *Rev. Mod. Phys.* **80**, 885 (2008).
- ¹¹ J. D. Sau, R. M. Lutchyn, S. Tewari, S. D. Sarma, Generic new platform for topological quantum computation using semiconductor heterostructures, *Phys. Rev. Lett.* **104**, 040502 (2010).
- ¹² R. M. Lutchyn, J. D. Sau, and S. D. Sarma, Majorana fermions and a topological phase transition in semiconductor-superconductor heterostructures, *Phys. Rev. Lett.* **105**, 077001 (2010).
- ¹³ P. Ghosh, J. D. Sau, S. Tewari, and S. D. Sarma, Non-Abelian topological order in noncentrosymmetric superconductors with broken time-reversal symmetry, *Phys. Rev. B* **82**, 184525 (2010).
- ¹⁴ J. D. Sau, S. Tewari, R. M. Lutchyn, T. D. Stanescu, and S. D. Sarma, Non-Abelian quantum order in spin-orbit-coupled semiconductors: Search for topological Majorana particles in solid-state systems, *Phys. Rev. B* **82**, 214509 (2010).
- ¹⁵ M. Sato, Y. Takahashi, and S. Fujimoto, Non-Abelian Topological Order in -Wave Superfluids of Ultracold Fermionic Atoms, *Phys. Rev. Lett.* **103**, 020401 (2009).
- ¹⁶ Y. J. Lin, R. L. Compton, A. R. Perry, W. D. Phillips, J. V. Porto, and I. B. Spielman, Bose-Einstein condensate in a uniform light-induced vector potential, *Phys. Rev. Lett.* **102**, 130401 (2009).
- ¹⁷ P. Wang, Z.-Q. Yu, Z. Fu, J. Miao, L. Huang, S. Chai, H. Zhai, and J. Zhang, Spin-orbit coupled degenerate Fermi gases, *Phys. Rev. Lett.* **109**, 095301 (2012).
- ¹⁸ J. Dalibard, F. Gerbier, G. Juzeliūnas, P. Ohberg, Colloquium: Artificial gauge potentials for neutral atoms, *Rev. of Mod. Phys.* **83**, 1523 (2011).
- ¹⁹ L. Huang, Z. Meng, P. Wang, P. Peng, S. Zhang, L. Chen, D. Li, Q. Zhou, and J. Zhang, Experimental realization of two-dimensional synthetic spinorbit coupling in ultracold Fermi gases, *Nat. Phys.* **12**, 540 (2016). However, the heating is still serious which prevents the observation of many body phenomena due to the Rashba SOC for the alkali atoms. So the physics observed in^{19,20} is still at single particle physics.
- ²⁰ Z. Meng, L. Huang, P. Peng, D. Li, L. Chen, Y. Xu, C. Zhang, P. Wang, and J. Zhang, Experimental observation of a topological band gap opening in ultracold Fermi gases with two-dimensional spin-orbit coupling, *Phys. Rev. Lett.* **117**, 235304 (2016).
- ²¹ Z. Wu, L. Zhang, W. Sun, X.-T. Xu, B.-Z. Wang, S.-C. Ji, Y. Deng, S. Chen, X.-J. Liu, and J.-W. Pan, Realization of two-dimensional spin-orbit coupling for Bose-Einstein condensates, *Science* **354**, 83 (2016). Indeed, the lifetime of SOC ⁸⁷Rb BEC was already made as long as 300ms in this work and improved to ~ 1 s recently, so the current experiment set-up the stage to observe any possible many body phenomena at a weak interaction where the heating rate is well under control.
- ²² O. Boada, A. Celi, J. I. Latorre, and M. Lewenstein, Quantum simulation of an extra dimension, *Phys. Rev. Lett.* **108**, 133001 (2012).
- ²³ A. Celi, P. Massignan, J. Ruseckas, N. Goldman, I. B. Spielman, G. Juzeliūnas, and M. Lewenstein, Synthetic gauge fields in synthetic dimensions, *Phys. Rev. Lett.* **112**, 043001 (2014).
- ²⁴ M. L. Wall, A. P. Koller, S. Li, X. Zhang, N. R. Cooper, J. Ye, and A. M. Rey, Synthetic spin-orbit coupling in an optical lattice clock, *Phys. Rev. Lett.* **116**, 035301 (2016).
- ²⁵ L. F. Livi, G. Cappellini, M. Diem, L. Franchi, C. Clivati, M. Frittelli, F. Levi, D. Calonico, J. Catani, M. Inguscio, L. Fallani, Synthetic dimensions and spin-orbit coupling with an optical clock transition, *Phys. Rev. Lett.* **117**, 220401 (2016).
- ²⁶ S. Kolkowitz, S. L. Bromley, T. Bothwell, M. L. Wall, G. E. Marti, A. P. Koller, X. Zhang, A. M. Rey, and J. Ye, Spinorbit-coupled fermions in an optical lattice clock, *Nature* **542**, 66 (2017).
- ²⁷ F. A. An, E. J. Meier, and B. Gadway, Direct observation of chiral currents and magnetic reflection in atomic flux lattices, arXiv:1609.09467.
- ²⁸ N. Q. Burdick, Y. Tang, and B. L. Lev, Long-lived spin-orbit-coupled degenerate dipolar Fermi gas, *Phys. Rev. X* **6**, 031022 (2016).
- ²⁹ F. Sun, J. Ye, W.-M. Liu, Quantum magnetism of spinor bosons in optical lattices with synthetic non-Abelian gauge fields, *Phys. Rev. A* **92**, 043609 (2015).
- ³⁰ We expect that the Pfaffian defined from the two discrete symmetries respectively at the four momenta are identical. It was known¹ that the Pfaffian is equal to the parity of the Chern number. Because, the TSF in Fig.1 has Chern number $C = 2$, so the Pfaffian can not be used to distinguish the trivial SF with $C = 0$ and the TSF with $C = 2$ in Fig.1.
- ³¹ F. Sun, X.-L. Yu, J. Ye, H. Fan, and W.-M. Liu, Topological quantum phase transition in synthetic non-abelian gauge potential: gauge invariance and experimental detections, *Sci. Rep.* **3**, 2119 (2013).
- ³² F. Sun and J. Ye, Type-I and type-II Weyl fermions, topological depletion, and universal subleading scaling across topological phase transitions, *Phys. Rev. B* **96**, 035113 (2017).
- ³³ In fact, by using the unitary transformation $U = e^{i\pi/2\sigma_z}$, one can reach the same Hamiltonian with the corresponding transformation in the two component spinor ϕ_L .

- ³⁴ Here, we are using the normalization $\{\gamma_i, \gamma_j\} = \delta_{ij}$ instead of the more conventional one $\{\gamma_i, \gamma_j\} = 2\delta_{ij}$ which seems more natural in the BdG equation normalization.
- ³⁵ J. Ye, Random Magnetic Field and Quasiparticle Transport in the Mixed State of High- T_c Cuprates, *Phys. Rev. Lett.* **86**, 316 (2001).
- ³⁶ J. Ye, Thermally generated vortices, gauge invariance, and electron spectral function in the pseudogap regime *Phys. Rev. Lett.* **87**, 227003 (2001).
- ³⁷ J. Ye, Quantum fluctuation generated vortices, dual singular-gauge transformation, and zero-temperature transition from d-wave superconductor to underdoped regime, *Phys. Rev. B* **65**, 214505 (2002).
- ³⁸ P. Medley, D. M. Weld, H. Miyake, D. E. Pritchard, and W. Ketterle, Spin gradient demagnetization cooling of ultracold atoms, *Phys. Rev. Lett.* **106**, 195301 (2011).
- ³⁹ S. Sugawa, K. Inaba, S. Tai, R. Yamakasi, M. Yamashita, and Y. Takahashi, Interaction and filling-induced quantum phases of dual Mott insulators of bosons and fermions, *Nature Phys.* **7**, 642 (2011).
- ⁴⁰ J. Ye, Emery-Kivelson Line and Universality of Wilson Ratio of Spin Anisotropic Kondo Model, *Phys. Rev. Lett.* **77**, 3224 (1996); Abelian bosonization approach to quantum impurity problems, *Phys. Rev. Lett.* **79**, 1385 (1997).
- ⁴¹ J. T. Stewart, J. P. Gaebler and D. S. Jin, Using photoemission spectroscopy to probe a strongly interacting Fermi gas, *Nature* **454**, 744 (2008).
- ⁴² C. H. Schunck1, Y. Shin, A. Schirotzek, W. Ketterle, Determination of the fermion pair size in a resonantly interacting superfluid, *Nature* **454**, 739 (2008).
- ⁴³ L. Tarruell, D. Greif, T. Uehlinger, G. Jotzu, and T. Esslinger, Creating, moving and merging Dirac points with a Fermi gas in a tunable honeycomb lattice, *Nature* **483**, 302 (2012).
- ⁴⁴ M. Aidelsburger, M. Lohse, C. Schweizer, M. Atala, J. T. Barreiro, S. Nascimbe, N. R. Cooper, I. Bloch, and N. Goldman, Measuring the Chern number of Hofstadter bands with ultracold bosonic atoms, *Nature Phys.* **11**, 162 (2015).
- ⁴⁵ N. Goldman, J. Dalibard, A. Dauphin, F. Gerbier, M. Lewenstein, P. Zoller, and I. B. Spielman, Direct imaging of topological edge states in cold-atom systems, *Proc. Natl. Acad. Sci.* **110**, 6736 (2013).
- ⁴⁶ N. Gemelke, X. Zhang, C. L. Huang, and C. Chin, In situ observation of incompressible Mott-insulating domains in ultracold atomic gases, *Nature* **460**, 995 (2009).
- ⁴⁷ Yu Y.-X., J. Ye, and W.-M. Liu, Coherence lengths in attractively interacting Fermi gases with spin-orbit coupling, *Phys. Rev. A* **90**, 053603 (2014).
- ⁴⁸ L. Jiang and J. Ye, Lattice structures of Fulde-Ferrell-Larkin-Ovchinnikov state, *Phys. Rev. B* **76**, 184104 (2007);
- ⁴⁹ J. Ye, Elementary Excitations, Spectral Weights and Experimental Signatures of a Supersolid and a Fulde-Ferrell-Larkin-Ovchinnikov State, *J. Low Temp Phys.* **160**(3), 71 (2010).
- ⁵⁰ L. Radzihovsky, Fluctuations and phase transitions in Larkin-Ovchinnikov liquid-crystal states of a population-imbalanced resonant Fermi gas, *Phys. Rev. A* **84**, 023611 (2011).
- ⁵¹ S.-S. Zhang, J. Ye, and W.-M. Liu, Itinerant magnetic phases and quantum Lifshitz transitions in a three-dimensional repulsively interacting Fermi gas with spin-orbit coupling, *Phys. Rev. B* **94**, 115121 (2016).
- ⁵² It was known that the finite momentum η pairing in the negative U Hubbard model is mapped to a FM in XY plane in the positive U case by a particle-hole transformation.
- ⁵³ C. A. Balseiro, L. M. Falicov, Superconductivity and charge-density waves, *Phys. Rev. B* **20**(11), 4457 (1979).
- ⁵⁴ Yu Y.-X., J. Ye, and W.-M. Liu, Goldstone and Higgs modes of photons inside a cavity, *Sci. Rep.* **3**, 3476 (2013).
- ⁵⁵ J. Ye and S. Sachdev, Superconducting, metallic, and insulating phases in a model of CuO2 layers, *Phys. Rev. B* **44**, 10173 (1991).
- ⁵⁶ F. Sun, J. Ye, W.-M. Liu, Quantum incommensurate skyrmion crystals and commensurate to in-commensurate transitions in cold atoms and materials with spinorbit couplings in a Zeeman field, *New Journal of Physics*, **19**(8), 083015 (2017).
- ⁵⁷ F. Sun, J. Ye, and W.-M. Liu, Classification of magnons in rotated ferromagnetic Heisenberg model and their competing responses in transverse fields, *Phys. Rev. B* **94**, 024409 (2016).
- ⁵⁸ F. Sun, J. Ye, and W.-M. Liu, Fermionic Hubbard model with Rashba or Dresselhaus spinorbit coupling, *New J. Phys.* **19**, 063025 (2017).
- ⁵⁹ F. Sun, J. Ye, and W.-M. Liu, In-commensurate Skyrmion crystals, devil staircases and multi-fractals due to spin orbit coupling in a lattice system, arXiv:1603.00451.
- ⁶⁰ The chemical potential means the Fermi energy only in the normal phase where $\Delta = 0$. However, when inside a SF, the particle number is not conserved, it can only be used to determine the average particle number.
- ⁶¹ L. Jiang and J. Ye, The mobility of dual vortices in honeycomb, square, triangular, Kagome and dice lattices, *J. Phys.: Condens. Matter* **18**, 6907 (2006).
- ⁶² J. Ye, Duality, magnetic space group and their applications to quantum phases and phase transitions on bipartite lattices in several experimental systems, *Nucl. Phys. B* **805** (3) 418 (2008).
- ⁶³ Y. Chen and J. Ye, Characterizing symmetry breaking patterns in a lattice by dual degrees of freedom, *Philos. Mag.* **92** 4484 (2012); Quantum phases, Supersolids and quantum phase transitions of interacting bosons in frustrated lattices, *Nucl. Phys. B* **869** 242 (2013).
- ⁶⁴ This is similar to the “order from quantum disorder” phenomena where infinite number of states are degenerate at the classical level, only quantum fluctuations can select the true quantum ground state from this classically degenerate manifold. For “order from quantum disorder” phenomena due to spin orbit coupling in a bipartite lattice, see F. Sun, J. Wang, J. Ye, and Y. Deng, arXiv:1711.06304; arXiv:1711.11580; arXiv:1712.06545.
- ⁶⁵ M. Takahashi, Half-filled Hubbard model at low temperature, *J. Phys. C: Solid State Phys.* **10**, 1289 (1977).
- ⁶⁶ See P. Ghaemi and F. Wilczek, Near-zero modes in superconducting graphene, arXiv:0709.2626.
- ⁶⁷ D.L. Bergman and K Le Hur, Near-zero modes in condensate phases of the Dirac theory on the honeycomb lattice, *Phys. Rev. B* **79**, 184520 (2009).
- ⁶⁸ X. Yang and S. Wan, Topological phase separation in trapped ultracold fermionic gases, *J. Phys. B* **45**, 065301 (2012).
- ⁶⁹ T. Fukui and Y. Hatsugai, Quantum spin Hall effect in three dimensional materials: Lattice computation of Z2 topological invariants and its application to Bi and Sb, *J. Phys. Soc. Jpn.* **76**, 053702 (2007).
- ⁷⁰ V. Schweikhard, I. Coddington, P. Engels, V. P. Mogen-dorff, and E. A. Cornell, Rapidly rotating Bose-Einstein

condensates in and near the lowest Landau level, Phys. Rev. Lett. **92**, 040404 (2004).